DEVELOPMENT AND SYNTHESIS OF MAGNETIC HIGH ENTROPY ALLOYS

HÜSEYİN BASRİ ÇERÇİ

SEPTEMBER 2022

ÇANKAYA UNIVERSITY

GRADUATE SCHOOL OF NATURAL AND APPLIED SCIENCES

DEPARTMENT OF MATERIALS SCIENCE AND ENGINEERING

MASTER'S THESIS IN

MICRO AND NANOTECHNOLOGY

DEVELOPMENT AND SYNTHESIS OF MAGNETIC HIGH ENTROPY ALLOYS

HÜSEYİN BASRİ ÇERÇİ

SEPTEMBER 2022

ABSTRACT

DEVELOPMENT AND SYNTHESIS OF MAGNETIC HIGH ENTROPY ALLOYS

ÇERÇİ, Hüseyin Basri

Master of Science in Micro and Nanotechnology

Supervisor: Assist. Prof. Dr. İlkay KALAY

September 2022, 84 pages

High Entropy Alloys (HEAs) are unique and new advanced metallic alloy systems, especially for aerospace and defense industries due to their superior and impressing mechanical, physical, electrical and magnetic properties. This thesis focuses on synthesis and development of magnetic HEAs and the investigation of magnetic properties, phase formation mechanisms, thermal stability, and mechanical properties of Fe-Co-Ni-Al-X (X= Ti, V, Nb) alloy systems under both as-cast and isothermally annealed conditions. The alloy designed were first done due to thermodynamic data calculations and then high purity elements were used to produce the alloys using vacuum arc melter. The high entropy alloys were characterized using X-ray diffraction (XRD), optic microscope (OM), scanning electron microscope (SEM), energy dispersive spectroscopy (EDS), vibrating sample magnetometer (VSM), and hardness tester.

The analysis shows the effect of constituent elements on the phase formation, magnetic and mechanical properties of Fe-Co-Ni-Al-X (X: Ti, V, Nb) alloy systems. It was found that the increase in Co concentration increases the magnetic saturation and decreases the coercive force. On the other hand, Cu and Ti has little significance on reducing the coercive force. The isothermal annealing processes are found to improve magnetic properties of the alloys. The isothermally annealed alloys at 928 K for 24 hours show phase t3ransformations in comparison to their as-cast and

isothermally annealed conditions at 928 K for 3 hours. The Vickers microhardness analysis show similar values for all as-cast alloys. The hardness values are found to increase with isothermal annealing of all alloys for 3 hours, but there are no significant changes for 24 hours isothermal annealing.

The analysis reveals the effect of Ti, V and Nb on microstructure and magnetic properties of Fe-Co-Ni-Al-X (X: Ti, V, Nb) alloy systems. Ti addition improves the magnetic properties of the alloys. V and Nb additions effect the microstructure and result in phase transitions of the alloys while the magnetic properties of the alloys are negatively affected by the addition of V and Nb.

Keywords: High Entropy Alloy, Magnetic Properties, Heat Treatment, Mechanical Properties

ÖZ

MANYETİK YÜKSEK ENTORPİLİ ALAŞIMLARIN GELİŞTİRİLMESİ VE SENTEZLENMESİ

ÇERÇİ, Hüseyin Basri
Mikro ve Nanoteknoloji Yüksek Lisans

Danışman: Dr. Öğr. Üyesi İlkay KALAY
Eylül 2022, 84 sayfa

Yüksek Entropili Alaşımlar (YEAlar), üstün ve etkileyici mekanik, fiziksel, elektriksel ve manyetik özellikleri nedeniyle özellikle havacılık ve savunma sanayileri için benzersiz ve yeni gelişmiş metalik alaşım sistemleridir. Bu tez, manyetik HEA'ların sentezi ve geliştirilmesine ve işlem görmemiş ve izotermal iyileştirme koşullarında ısıl işleme tabi tutulmuş Fe-Co-Ni-Al-X (X= Ti, V, Nb) alaşım sistemlerinin manyetik özelliklerinin, faz oluşum mekanizmalarının, termal kararlılığının ve mekanik özelliklerinin araştırılmasına odaklanmaktadır. Alaşımlar öncelikle termodinamik veri hesaplamalarına dayanarak tasarlanmış ve daha sonra tasarlanan alaşımlar yüksek saflıkta elementler kullanılarak vakumlu ark eritici ile üretilmiştir. Yüksek entropili alaşımlar, X-ışını kırınımı (XRD), optik mikroskop (OM), taramalı elektron mikroskobu (SEM), enerji dağılımlı spektroskopi (EDS), titreşimli numune manyetometresi (VSM) ve sertlik test cihazı kullanılarak karakterize edilmiştir.

Sonuçları, bileşen elementlerin Fe-Co-Ni-Al-X (X: Ti, V, Nb) alaşım sistemlerinin faz oluşumu, manyetik ve mekanik özellikleri üzerindeki etkisini göstermektedir. Co konsantrasyonundaki artışın manyetik doygunluğu arttırdığı ve zorlayıcı kuvveti azalttığı bulunmuştur. Öte yandan, Cu ve Ti'nin zorlayıcı kuvveti azaltmada çok az etkisi vardır. İzotermal tavlama işlemlerinin, alaşımların manyetik

özelliklerini iyileştirdiği ortaya çıkmıştır. 928 K'de 24 saat izotermal tavlanmış olan alaşımlar, döküm sonrası ve 928 K'de 3 saat izotermal tavlanmış durumlarına kıyasla faz dönüşümleri göstermektedir. Vickers mikrosertlik analizi, tüm döküm alaşımlar için benzer değerler sunmuştur. Tüm alaşımların 3 saat izotermal tavlama ile sertlik değerlerinin arttığı, ancak 24 saat izotermal tavlama için önemli bir değişiklik olmadığı görülmüştür.

Analiz, Ti, V ve Nb'nin Fe-Co-Ni-Al-X (X: Ti, V, Nb) alaşım sistemlerinin mikroyapısı ve manyetik özellikleri üzerindeki etkisini ortaya koymaktadır. Ti ilavesi, alaşımların manyetik özelliklerini geliştirmektedir. V ve Nb ilaveleri alaşımların mikro yapısını etkileyerek faz geçişlerine neden olurken, V ve Nb ilavelerinin alaşımların manyetik özelliklerini olumsuz yönde etkilediği sonucuna varılmıştır.

Anahtar Kelimeler: Yüksek Entropi Alaşımı, Manyetik Özellikler, Isıl İşlem, Mekanik Özellikler

To My Precious Family

ACKNOWLEDGMENTS

First of all, I would like to express my sincere thanks to my thesis supervisor, Assistant Professor İlkay KALAY for her support, guidance, knowledge, and support throughout my undergraduate and graduate studies and became the guide of the study presented here.

I would like to express my gratitude and thanks to Professor Y. Eren KALAY for his help and wisdom during my graduate studies.

I want to express my profound thanks to Assistant Professor Gökhan POLAT. Throughout this period, he helped me in many ways and shared his knowledge and opinions about my studies.

I would like to express my deepest gratitude to my brother Sezer Can ÇERÇİ, who helped me both physically and morally during this process.

I would like to express my gratitude and warm thanks to my laboratory friends, Süleyman Batuhan ARSLAN, Fatih Sina KAYIR, and Yunus Emre ÜNSAL, who helped me with the experiments and studies.

I would like to thank my colleagues Bahadır TATAR, Ayber Eray ALGÜNER, and Şeyda Anıl HÖKE for being with me and keeping their friendship throughout this process.

TABLE OF CONTENTS

LIST OF TABLES

LIST OF FIGURES

LIST OF ABBREVIATIONS AND SYMBOLS

HEA	High Entropy Alloys
BCC	Body Centered Cubic
FCC	Face Centered Cubic
XRD	X-Ray Diffraction
SEM	Scanning Electron Microscope
EDS	Energy Dispersive Spectroscopy
VSM	Vibrating Sample Magnetometer
H_c	Coercive Force
M_r	Residual Magnetism
M_s	Magnetic Saturation
HV	Hardness Vickers
nm	Nano Meter
μm	Micro Meter

CHAPTER I

1. INTRODUCTION

1.1 METALLIC ALLOYS

The history of metals and metallic alloys has been started since the early ages with the discovery of new metals with unique properties. The first metallic alloys, copper alloys were discovered and used in the bronze age [1]. The development of metallic alloys has been highly demanded with the increase in the requirements of better mechanical, electrical, magnetic, optic, thermal, physical and chemical properties Development of metallic alloys results in in the enhancement of new alloying techniques. The most widely used alloying technique is based on the alloying of principle elements, such as copper, iron, nickel, aluminum, and similar elements, in higher concentrations with other elements in minor amounts [2]. The needs for more efficient and advanced production steps, higher production rates of metallic alloys have increased the demands for new alloying techniques [3]. The design of proportions of alloying elements is another important step during the production of alloys. For instance, by the addition of silicon and/or magnesium, the strength of aluminum varies significantly or by reducing the carbon concentration, more ductile and durable steels can be produced. The emerging developments in industry and technology, as well as increasing engineering necessities, play a major role in the design and development of new alloy types. The development of complex and strong new-generation alloys has gained great importance in recent years.

1.2 HIGH ENTROPY ALLOYS

Regarding the demands of new alloy systems with improved mechanical, physical, thermal and magnetic properties especially in aviation and defense industry, the invention of high entropy alloys (HEAs) have attracted tremendous attention [4]. Since their discovery by Cantor and Yeh in 2004, much efforts have been given to develop and design new HEA systems due to their unique mechanical such as high strength and hardness, thermal, magnetic, high temperature mechanical

properties and superior corrosion and oxidation resistance. The new generation HEAs are known as alloys consist of five or more principal elements in equiatomic or nearly equiatomic proportions. The concentrations of the constituent elements should be between 5 and 35% atomic percentage[3]–[6]. The first HEA produced by Cantor et al in 1981 was equiatomic CoCrFeMnNi alloy which is known as Cantor alloy [3], [7]. Even the system has 5 principal elements, it had a single-phase solid solution. The single-phase structure of multi component alloy attracted much attention. J. W. Yeh started working on this new alloy system and developed a concept highlighting the importance of increasing the mixing entropy of the system[3]. Yeh published the first article in 2004 on the concepts of alloy design of high entropy alloys which had a high impact on the development of these new next generation alloy systems. The research on the design and development of HEAs have revealed the superior properties of the alloys, such as mechanical, thermal, electrical, and magnetic. The Ashby diagram in Figure 1.1 indicates higher fracture toughness and yield strength values for HEAs than that of the other conventional engineering materials [7]. The recent studies have also shown the high thermal stability, high hardness and strength, excellent wear resistance, enhanced electrical properties, innovative magnetic properties, and high corrosive resistance of HEAs [5] due to their unique solid solution formation capabilities with simple crystal structures such as Face Centered Cubic (FCC) and/or a Body Centered Cubic (BCC).

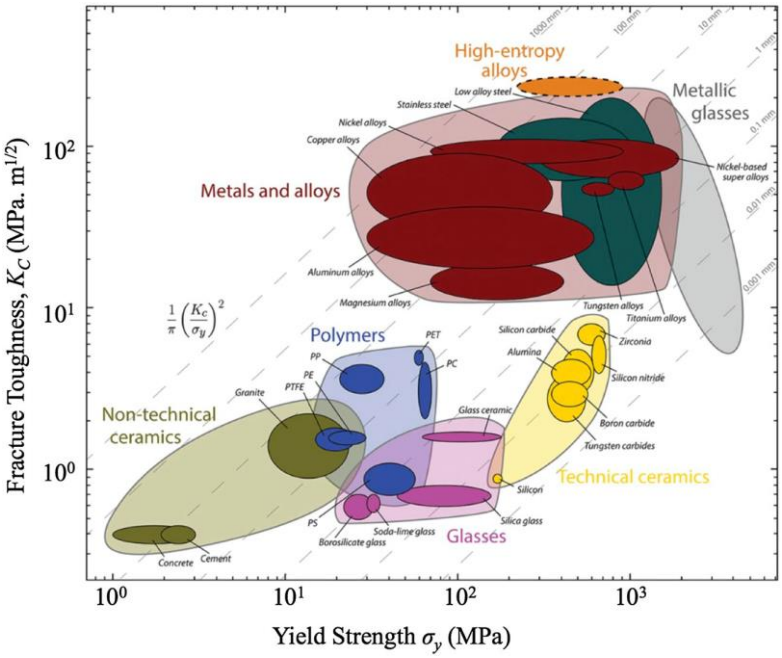

Figure 1.1: Ashby diagram of the fracture toughness versus the yield strength [7].

The phase formation mechanisms especially the solid solution characteristics of HEAs depend on thermodynamic and Hume-Rothery rules. However, Hume-Rothery rules are not enough alone for explaining the single solid solution formation, thus thermodynamic empirical parameters have to be considered in phase selection and formation mechanisms of HEAs. The maximum number of possible phases in a system can be calculated using Gibbs' phase rule given in equation 1 [8].

$$P + F = C + 1 \tag{1.1}$$

where F is the degrees of freedom, C is the number of elements, and P is the number of phases formed. The maximum number of possible phases in an alloy, which contains C number of elements, can be obtained using Gibbs phase rule. According to Equation 2, binary alloys may either form a solid solution or the solution with the intermetallic phases [1].

$$A + B = AB_{solidsolution}: \Delta G_{mix} = \Delta H_{mix} - T\Delta S_{mix} \tag{1.2}$$

where ΔG_{mix} is the Gibbs free energy, $\Delta H_{mix}$is the mixing enthalpy, T is the temperature, and $\Delta S_{mix}$is the entropy value. Gibbs Free Energy thermodynamically determines the phase stability and selection of multi components alloy systems. Figure 1.2 indicates different possibilities of phase formation in ternary alloys with different configurations due to Gibbs Free Energy. The minimum Gibbs Free Energy and maximum mixing entropy determines the equilibrium condition for the alloys. Particularly, for the formation of solid solution phases in HEAs, the maximum level of disorderness should be achieved by combining at least 5 principal elements.

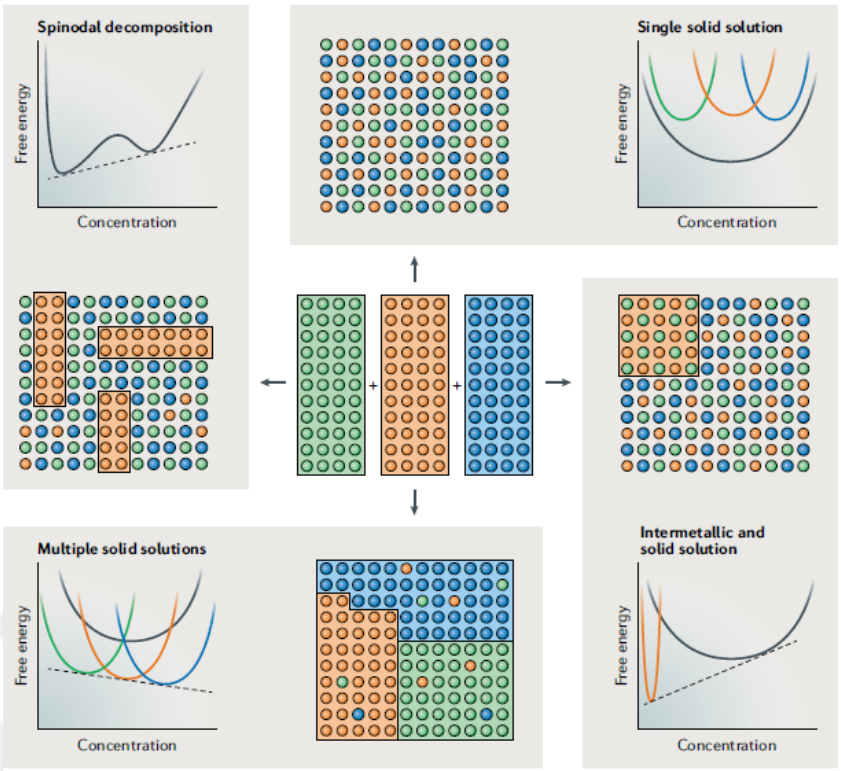

Figure 1.2: Possible mixing reactions for three alloying elements. Some of the possible reactions that can occur when three different elements, represented by the red, blue and green spheres, are mixed in equal proportions, including spinodal decomposition, formation of single or multiple solid solutions or precipitation of an intermetallic compound in a solid solution [1].

The high entropy criteria of HEAs based on the magnitude of configurational entropy. The change in the configurational entropy per mole for an alloy system with n components can be calculated from the following equation

$$\Delta S_{conf} = -R \sum_{i=1}^{n} x_i \ln x_i \tag{1.3}$$

Where R is the gas constant, x_i is the mole fraction of the n^{th} element. Due to the change in configurational entropy of mixing, the alloy systems can be classified. Table 1.1 indicates the dependency of ΔSconf on the number of components. It was mentioned previously that the alloy will be categorized as low entropy when ΔSconf is less than 0.69R, the alloy will be named as medium entropy when ΔSconf is between 0.69R and 1.61R, and the alloy will be classified as high entropy when ΔSconf is greater than 1.61R.

Table 1.1: The change in configurational entropy with respect to the number of components in the alloy.

n	1	2	3	4	5	6	7	8
ΔS_{conf}	0	0.69R	1.1R	1.39R	1.61R	1.79R	1.95R	2.08R

The enthalpy of mixing (ΔH_{mix}) is used to calculate Gibbs free energies of the HEAs can be determined using the following relationship:

$$\Delta H_{mix} = \sum_{i=1}^{n} x_i \overline{\Delta H_i} \tag{1.4}$$

Where $\overline{\Delta H_i}$ is the partial molar enthalpy of i^{th} element and can be calculated using the following relationship:

$$\overline{\Delta H_i} = \sum_{i=1\ j\neq i}^{n} 4 x_i x_j H_{ij} \tag{1.5}$$

Where x_i, x_j, and H_{ij} are the molar ratios of the i^{th} and j^{th} elements, the enthalpy of mixing value of binary element systems, respectively. The mixing enthalpy values of binary systems are given in the Table 1.2. The Gibbs free energies of the HEAs can be determined using mixing entropy and mixing enthalpy to estimate the phase formation.

Table 1.2: Enthalpy matrix containing the enthalpies of formation of the lowest energy structure of each binary compound [7].

	Mg	Al	Ti	V	Cr	Mn	Fe	Co	Ni	Cu	Zr	Nb	Mo	Ru	Rh	Pd	Ta	W
Mg	0	-33	20	171	160	87	77	-31	-723	-147	-31	105	164	4	-478	-742	122	234
Al	-33	0	-428	-282	-138	-278	-369	-629	-677	-224	-539	-288	-168	-678	-1101	-874	-320	-16
Ti	20	-428	0	37	**-372**	-277	-418	-386	-435	-147	24	11	-167	-763	-790	-646	31	-82
V	171	-282	37	0	-88	-286	-176	-199	-250	13	26	-56	-127	-321	-393	-275	-122	-97
Cr	160	-138	**-372**	-88	0	-110	-8	5	-30	108	**-150**	**-47**	42	4	-129	-82	-130	26
Mn	87	-278	-277	-286	-110	0	9	-19	-115	29	-192	-153	-138	-15	-188	-251	-254	-92
Fe	77	-369	-418	-176	-8	9	0	-60	-97	65	-290	-2505	-484	41	-57	-116	-3468	-554
Co	-31	-629	-386	-199	5	-19	-60	0	-21	54	-324	-178	-52	52	12	-10	-253	-84
Ni	-723	-677	-435	-250	-30	-115	-97	-21	0	-6	-463	-316	-100	40	2	-6	-746	-11
Cu	-147	-224	-147	54	108	29	65	54	-6	0	-169	-29	83	108	-4	-126	28	129
Zr	-31	-539	24	26	**-150**	-192	-290	-324	-463	-169	0	21	-138	-644	-811	-816	36	-14
Nb	105	-288	11	-56	**-47**	-153	-2505	-150	-316	-29	21	0	-133	-249	-548	-435	-10	-76
Mo	164	-168	-167	-127	42	-136	-484	-52	-100	83	-138	-133	0	-57	-248	-100	-193	-8
Ru	4	-678	-763	-321	4	-15	41	52	40	108	-644	-249	-57	0	-8	47	-332	-66
Rh	-478	-1101	-790	-393	-129	-188	-57	12	2	-4	-811	-548	-248	-8	0	37	-611	-27
Pd	-742	-874	-646	-275	-82	-251	-116	-10	-6	-126	-816	-435	-100	47	37	0	-480	-12
Ta	122	-320	31	-122	-130	-254	-3468	-253	-746	28	36	-10	-193	-332	-611	-480	0	-114
W	234	**-161**	-82	-97	26	-92	-554	-84	-116	129	-145	-76	-8	-66	-273	-123	-114	0

Energy scale [meV/atom]

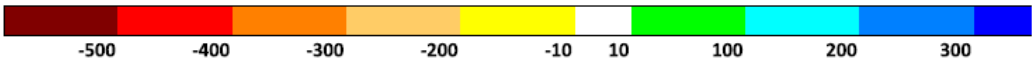

The phase formation mechanism of HEAs are affected by thermodynamical empirical parameters and Hume-Rothery rules. The physical parameters due to Hume-Rothery rules are given as atomic radii difference (δ) between constituent elements, crystal structure, electronegativity (X) and Valence Electron Concentration (VEC) values which can be determined using the following relationships,

$$\delta = \sqrt{\sum_{i=1}^{n} c_i \left(1 - \frac{r_i}{\bar{r}}\right)^2} \tag{1.6}$$

where n is the total number of components I and $\bar{r}$, the average atomic radius of the alloy and given in the following relationship,

$$\bar{r} = \sum_{i=1}^{n} c_i r_i \tag{1.7}$$

Where r_i and c_i are the atomic radii and concentration of the i^{th} element respectively. The electronegativity difference of the alloy can be calculated by

$$\Delta X = \sqrt{\sum_{i=1}^{n} c_i \left(1 - \frac{X_i}{\bar{X}}\right)^2} \tag{1.8}$$

Where $\bar{X}$, the average electronegativity, and is given below,

$$\bar{X} = \sum_{i=1}^{n} c_i X_i \tag{1.9}$$

Where X_i is the electronegativity of the i^{th} element. The VEC number of the alloy systems can be calculated by using the following equation

$$VEC = \sum_{i=1}^{n} c_i (VEC)_i \tag{1.10}$$

Where $(VEC)_i$ is the VEC of the i^{th} element.

According to Hume-Rothery rules, the solid solution forms when the atomic radii differences less than 15%. For the complete solid solubility of alloys, the atomic radii difference should be less than. In addition to the atomic radii differences, electronegativities of the constituent elements must be similar to each other.

Furthermore, VEC of elements in the alloy must be similar or nearly equal to each other in order to prevent intermetallic compound formation. The VEC value is correlated well with the crystal structure and phase stability of the HEAs. It was reported that when VEC ≤ 6.87, BCC solid solution is stable, when 6.87 ≤ VEC ≤ 8.0, the dual phase of BCC+FCC is achieved and when VEC ≥ 8.0, the stable solid solution phase is FCC. [9]. Even the solid solution phase formation is specific to and the unique property of HEAs, it might be possible to achieve intermetallic compounds (IC) in HEAs. Due to the previous studies, it was reported that the presence of ICs in a solid solution matrix can enhance the mechanical properties of HEAs. The predicted phase formation of HEAs due to the thermodynamically estimated parameters are given in Table 1.3.

Table 1.3: The thermodynamic parameters and phase formation relationships of HEAs.

Thermodynamic Parameter	**Condition**	**Possible Phase(s)**
THE ENTROPY of MİXİNG ($\Delta S_{MİX}$)	$11 \leq \Delta S_{mix} \leq 19.5$ kJ/mol	Solid solution formation
ENTHALPY of MİXİNG ($\Delta H_{MİX}$)	$-22 \leq \Delta H_{mix} \leq 7.5$ J/k.mol	
ATOMİC SİZE DİFFERENCES (Δ)	$\Delta \leq 8.5$	
VALANCE ELECTRON CONCENTRATİON (VEC)	VEC ≤ 6.87	BCC
	6.87 ≤ VEC ≤ 8.0	BCC+FCC
	8.0 ≤ VEC	FCC

The crystal structure and lattice constants give significant structural information about HEAs. XRD analysis is used to determine the structure, phase stability and lattice constants of the phases. Thee lattice constants of the cubic systems can be determined using the combined equation of Bragg's Law and the interplanar spacing, d_{hkl}, as a function of Miller indices and lattice parameters in cubic system given in following relationships, respectively

$$n\lambda = 2d_{hkl} \sin\theta \tag{1.11}$$

Where n is the order of reflection, λ is the wavelength of x-ray, and θ is the angle between the incident x-ray beam and the plane of atoms.

$$d_{hkl} = \frac{a_o}{\sqrt{h^2+k^2+l^2}} \quad (1.12)$$

1.2.1 The Four Core Effect

Four critical factors affecting the phase formation, microstructure and thus the properties of HEAs were reported in the literature. These four core effects are given as e high entropy, severe lattice distortion, cocktail, and sluggish diffusion effects [3]. The unique physical, thermal, mechanical, and magnetic properties are all depending on these four core effects.

1.2.1.1 High Entropy Effect

High Entropy effect concept postulates that the increased mixing configurational entropy due to the high number of constituent elements decreases the free energy of solid solution phases and thus the formation of solid solution easily occurs. The Gibbs phase rule indicates that, the possible phase formation increase depends on number of the elements in the system [8] and this results in the formation of binary, ternary, or quaternary compounds in multicomponent alloys. However, this situation can be neglectable for HEAs due to their high mixing entropy. Although the HEAs have larger mixing entropy than conventional alloys, their enthalpy of mixing, atomic radii differences, electronegativities, and VEC are also critical for solid solution formation. The selection of compositions of HEAs is very critical to achieve solid solution otherwise the intermetallic compounds may form. Table 1.2 shows the conditions for solid solution formation.

1.2.1.2 Severe Lattice Distortion Effect

The severe lattice distortion effect is founded on the concept that presence of the different sizes of the constituent elements results in lattice strains and thus [10]. The distortion caused by the atomic radii differences in the lattice structure is illustrated in Figure 1.4. Even though Hume-Rothery rules specify the atomic radii of each element which should be similar to each other, high number of elements in the HEAs tend to decrease the average atomic radii difference in HEAs. Figure 1.5 indicates the severe lattice distortion effect in BCC structure. The amount of lattice distortions effect the electrical, thermal and mechanical properties such as hardness and strength of the alloys [3], [11].

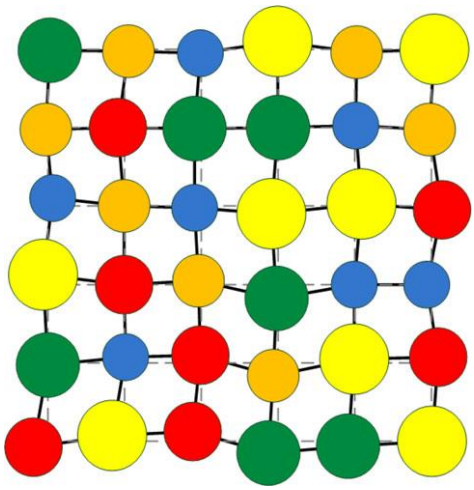

Figure 1.3: Lattice distortion of the multi-element system [11].

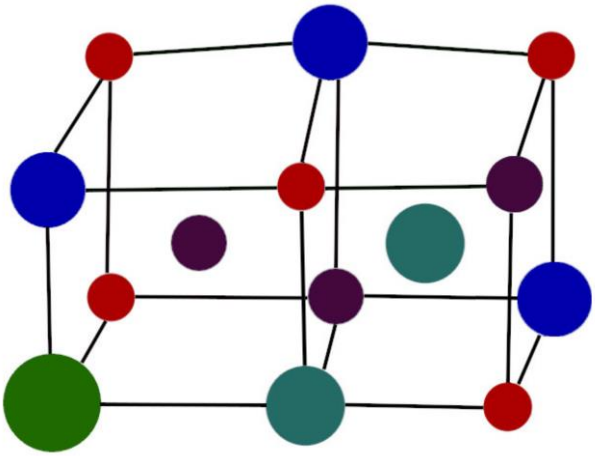

Figure 1.4: Schematic representation of lattice distortion effect on the BCC structure [12].

1.2.1.3 Cocktail Effect

The cocktail effect relies on the relationship between the mixture of constituent elements and the properties of the HEAs [3].HEAs may have single or multi-phase structure due to the composition and the production technique. HEAs have multi-component systems, thus the structure of HEAs can be interpreted as atomic scale composites. The number of constituent elements effect the mechanical, thermal, electrical, and magnetic properties of HEAs. Figure 1.5 shows the effect of Al concentration on the hardness of $Al_xCoCrCuFeNi$ HEA system. It was reported that the increase in Al results in the structural transition from FCC to FCC+BCC to BCC phases in $Al_xCoCrCuFeNi$ HEA thus increases the hardness of the alloy. It was reported that MoNbTaW and MoNbTaVW alloys have higher melting points and

higher softening resistance than Ni- and Co-based superalloys due to the cocktail effect [3].

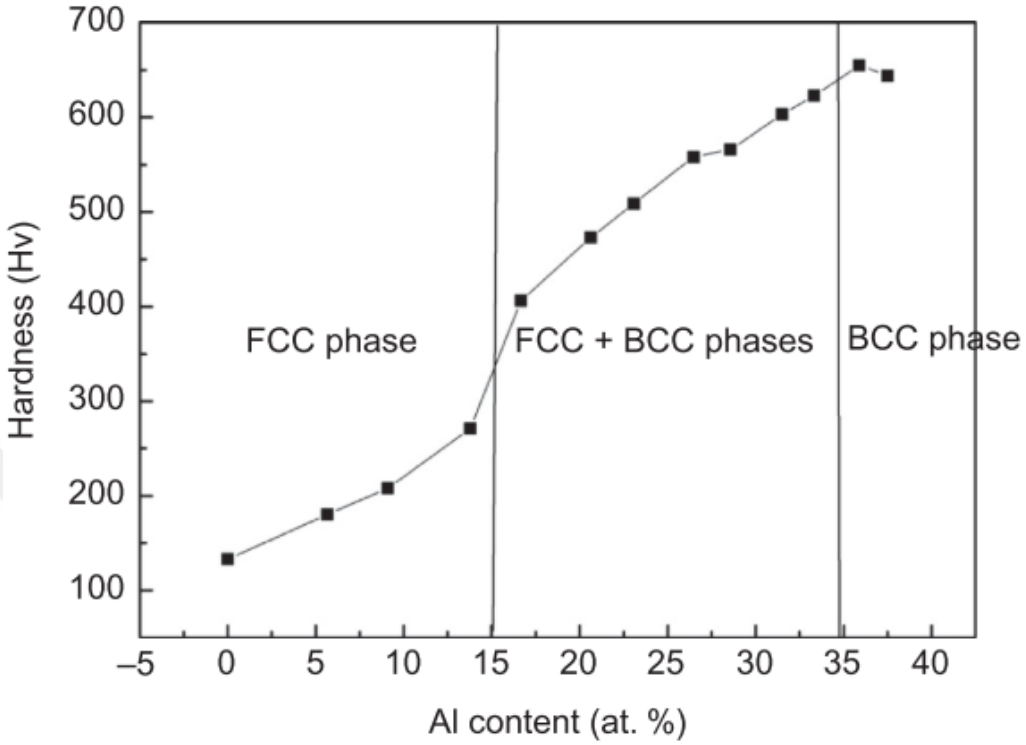

Figure 1.5: Cocktail effect introduced by the interaction of constituent elements in the $Al_xCoCrCuFeAl$ alloy [3].

1.2.1.4 Slugish Diffusion Effect

Due to their multi-principal element characteristic, HEAs show diffusion rates. The new phase formation requires the cooperative diffusion of atoms to their new lattice sites. However, each atom has different kinds of neighbor atoms with different sizes, thus it makes the diffusion process hard in HEAs. Due to randomness in the atomic configuration, and the presence of different kinds of local bonds, different local energies will present [10].Due to sluggish diffusion effect, HEAs have high-temperature strength, high-temperature structural stability, and a tendency to form nanoscale structures [8], [12]. The diffusion process requires the movement of atoms when sufficient energy is satisfied [13]. Even the diffusion mechanism is same for HEAs, different kinds of neighboring, slows down the diffusion process.

1.3 MAGNETISM AND MAGNETIC MATERIALS

The history of magnetism and magnetic materials has begun with discovery of the first magnetic material Magnetite (Fe_2O_3). The word of magnet was etymon from "the stone from Magnesia" [14], [15]. Magnetism and magnetic materials are used in many electronic and computational devices in today's technology [16]. The research on magnetism and magnetic materials is interdisciplinary subject [15].

1.3.1 Magnetism

Magnetism is a phenomenon caused by the repulsive or attractive forces exerted by a material on a different or a similar material [13]. William Gilbert worked on magnetism, and published the first book titled as "*On the Magnet*" book in 1600 [14]. Hans Christian Oersted discovered the magnetic field, produced by an electric current, in 1820. In the light of this discovery, first electromagnets were produced in 1825 [14].

1.3.1.1 Magnetic Poles

Attractive or repulsive forces can be observed with using two magnets. Magnetic poles on magnets are shown in Figure 1.6. The attractive forces are generated for the opposite poles while the repulsive forces are generated for the same poles [14]. These regions, which are formed at the two ends of any magnet, are called the north and south poles similar to the geographical poles of the earth. After the magnet is induced, it will have permanent magnetic poles that cannot be removed by divided into the smaller pieces. That is, no matter how small the piece is broken up into, it always has two poles.

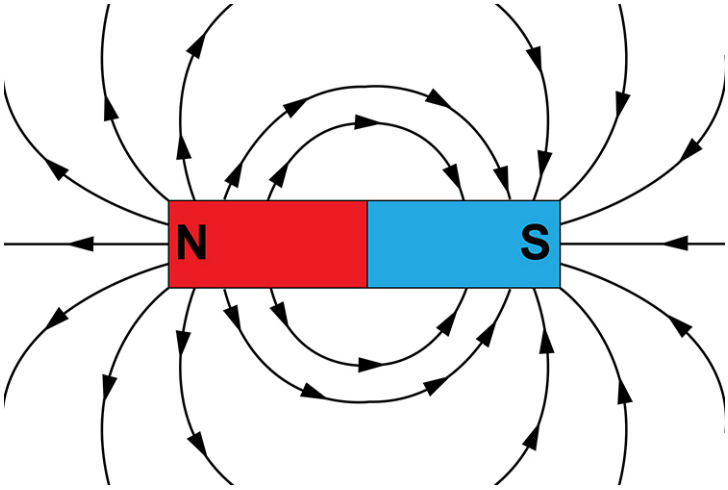

Figure 1.6: A bar magnet with magnetic field lines.

1.3.1.2 Magnetic Dipoles

Magnetic forces are generated by the movement of charged particles such as electrons [13]. The dipoles formed by the north and south poles, are found in all materials that produce magnetic fields. A magnetic dipole can be thought of as the fundamental observable unit of magnetism. The dipole can be described as a part that consists of two equal but opposite poles, and interaction between these two charged monopoles creates a vectoral force field in the space, known as the magnetic field. The most commonly known examples of magnetic dipoles include bar magnets, electrons, and planet Earth.

1.3.1.3 Magnetic Moment

Motion of electrons in an atom creates an atomic scale magnetism. The macro scale magnetic properties are made up by combining all these atoms [13]. The magnetic moment of each electron in atoms is based on two sources:

1) Orbital motion: The motion of the electron in an orbit around the nucleus.

2) Spin motion: The rotational motion of the electron around itself while moving in the orbit.

The magnetic field around the electron is generated by the summation of both orbital and spin motions. The summation of magnetic moment of electrons in atoms can create two different results due to their spin motion:

1) The magnetic moments of all the electrons are so oriented that they cancel one another out, and the atom has no net magnetic moment. This condition leads to diamagnetism.

2) The cancellation of electronic moments is only partial, and the atom is left with a net magnetic moment. Such an atom is often referred to, for brevity, as a magnetic atom. Substances composed of atoms of this kind are para-, Ferro-, Antiferro-, or Ferrimagnetic [14].

These two possibilities constitute the types of magnetism seen in materials.

1.3.1.4 Diamagnetism

The summation of electron motions creates no net magnetic moments on atoms in diamagnetism. Although there are no net magnetic moments in diamagnetism, the atoms create a magnetic moment opposite to applied magnetic field, shown in Figure 1.7 [13], [14]. Diamagnetism is a weak form of magnetism, it is not permanent and only observed when an external magnetic field is applied [13].

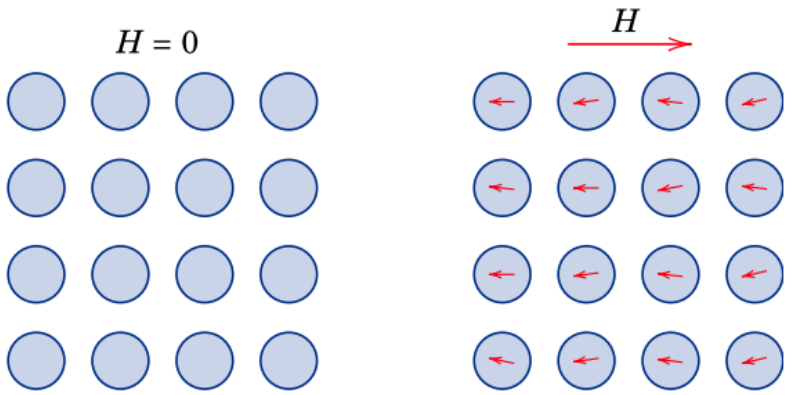

Figure 1.7: Atomic dipole configuration due to magnetic field in diamagnetic material [13].

1.3.1.5 Paramagnetism

When the summation of electron motions creates a net magnetic moment on atom, it is named as paramagnetism. For some of the solids, the magnetic moment of electrons can't be canceled by each other because of the incomplete electron shells and this situation is result to a net magnetic moment in atoms [13]–[15]. Electron shells close to the nucleus in atoms usually complete their electron configurations, so they show a diamagnetic effect. Although paramagnetic atoms are responded to an external magnetic, in contrast to diamagnetic atoms, it has same direction with the

magnetic field vector shown in Figure 1.8. Although the magnetic moments of atoms respond oppositely to external magnetic field in diamagnetism, the magnetic moments of atoms direct to same direction with external magnetic field in paramagnetism [13]. Although incomplete electron shells cause to paramagnetism, there is a complex situation about incomplete outer shell. As can be seen in Table 1.4, Cu atoms have incomplete shell in their electronic structure. Although there is an incomplete shell in their electronic configuration, Cu atoms exhibit diamagnetism due to their completed inner shells.

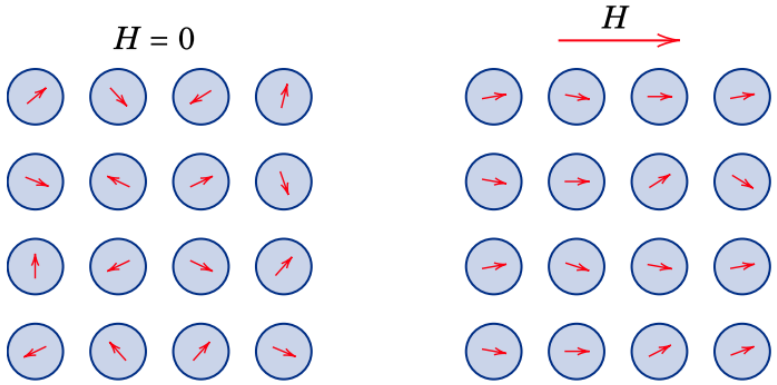

Figure 1.8: Atomic dipole configuration due to magnetic field in paramagnetic material [13].

Table 1.4: Electronic structures and magnetism types of Mn, Ni, and Cu elements.

Element	1s	2s	2p	3s	3p	3d	4s	Magnetism Type
Manganese	2	2	6	2	6	5	2	Paramagnetism
Nickel	2	2	6	2	6	8	2	Ferromagnetism
Copper	2	2	6	2	6	10	1	Diamagnetism

1.3.1.6 Ferromagnetism

Some of the transition metals such as Fe, Ni, Co, and some of the rare earth metals exhibit strong and permanent magnetization [13]. Even if the external magnetic field is removed, these metals exhibit magnetic properties. These are the characteristics of ferromagnetism [13]. Ferromagnetic materials exhibit permanent magnetic moments due to incomplete inner electron shells, even in the absence of an external magnetic field [13]. There are small regions caused by the alignment of magnetic moments of atoms in ferromagnetic materials. These regions are named as magnetic domains, and both ferromagnetic and ferrimagnetic materials possess them.

Ferromagnetic materials possess many small domains at the demagnetized states, and these domains are not aligned with each other. After the magnetization is begun, as can be seen in Figure 1.9, these small regions start to align with direction of external magnetic field, and all small domains are aligned and became whole at the end of magnetization [14]. The maximum possible magnetization occurs when all dipoles in the material are in the same direction as an external magnetic field. The saturation magnetization is equal to the product of the net magnetic moment for each atom and the number of atoms present. For each iron, cobalt, and nickel, the net magnetic moments per atom are 2.22, 1.72, and 0.60 Bohr magnetons, respectively [13]

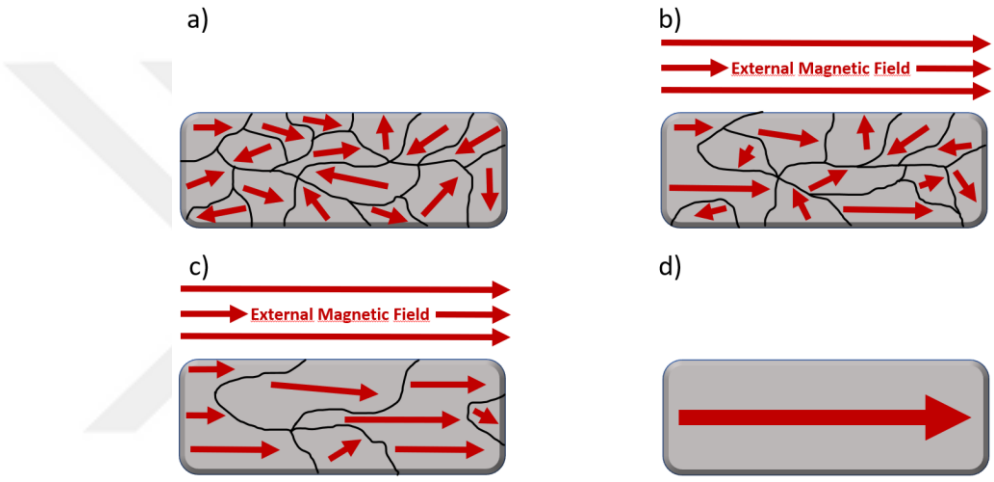

Figure 1.9: Behavior of ferromagnetic materials under external magnetic field. a) Orientation of magnetic domains in the absence of any magnetic field, b) when the magnetic field is applied, c) when the magnetic field stays for a certain time, and d) when the magnetic field is removed.

1.3.1.7 Antiferromagnetism

In contrast to ferromagnetism, magnetic moments of atoms are in exactly opposite directions in Antiferromagnetism [13]–[15]. Although there is no net magnetic moment in macro scale, atoms possess net magnetic moment[13]. Manganese oxide (MnO), which is one of the antiferrimagnetic material, composed of Mn+2 and O-2 ions. O2+ ions do not have net magnetic moments due to total cancelation of both spin and orbital moments. Although Mn2+ ions show net magnetic moment, net magnetic moment in macro scale cannot be observed, because magnetic moments of Mn2+ ions are canceled to each other cause by exact opposite directions of them [13].

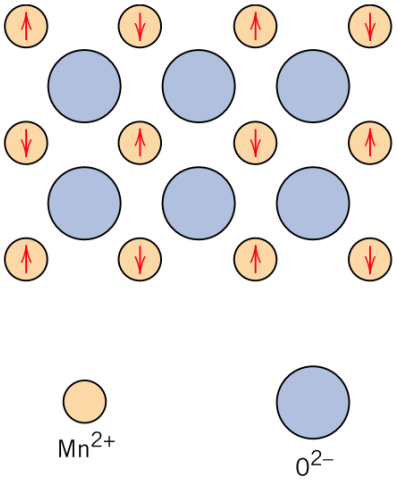

Figure 1.10: Schematic representation of the magnetic structure of the Manganese Oxide crystal [13].

1.3.1.8 Ferrimagnetism

Although ferrimagnetism has a net magnetic moment in macro scale similar to ferromagnetism, it has oppositely directed magnetic moments in atomic scales [13]. There is a such lesser magnetic moments than ferromagnetism in macroscale due to one of the oppositely directed moments is lower. As can be seen in Figure 1.11, magnetic moment orientation of a ferrimagnetic material has two oppositely directions.

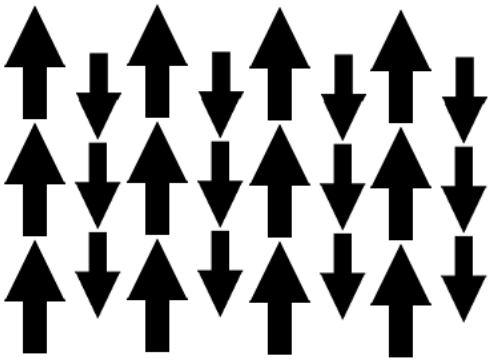

Figure 1.11: Schematic representation of Ferrimagnetism.
Figure 1.12

1.3.1.9 Magnetic Domains

Ferromagnetic materials have magnetic regions and these micro scale regions are formed by magnetic moments in the same directionz However, ferrimagnetic materials have two oppositely directed moments, magnetic domains observe due to

net magnetic moment in system. These domains can be observed below the Currie Temperature (T_c).

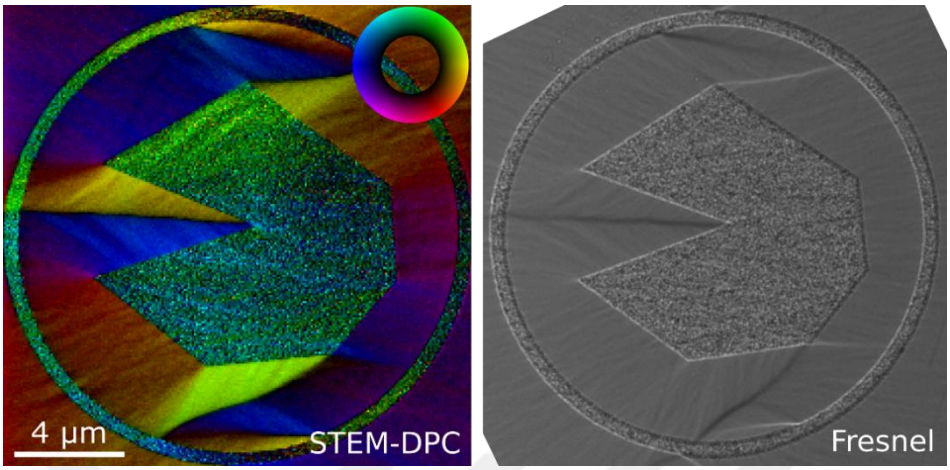

Figure 1.13: Scanning transmission electron microscopy (STEM) differential phase contrast (DPC) and Fresnel images of a Pacman shape milled in a permalloy thin film by the focused ion beam method. The two Lorentz microscopy techniques show complementary information regarding the magnetic domain structure surrounding Pacman. Image(s) acquired during student lab for the course Nanotools at the Norwegian University of Science and Technology (NTNU), with full permission for publishing given by students (Konarboland, A. and Tokle, E. Y. and Femoen, V. J.).

1.3.1.10 Hysteresis Loops

Shape, size, and directions of magnetic domains can change with applying a magnetic field on a magnetic material. As can be seen in Figure 1.13, magnetic domains become whole due to increasing in applied magnetic field strength. When all the magnetic domains oriented and became whole, magnetic saturation can reach. Magnetic field strength (H) and magnetic flux density (B) or magnetization (M) are not proportional to each other for ferro and ferrimagnetic materials [13].

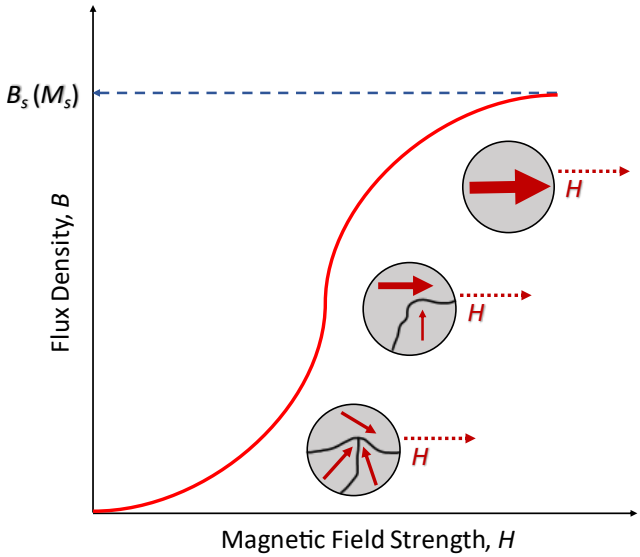

Figure 1.14: The B-versus-H behavior for a ferromagnetic or ferrimagnetic materials.

After that, magnetic field strength is reduced by changing the direction of magnetic field. Although, a reduction occurs in the magnetic field strength, the B-H curve doesn't follow the same path. When the magnetic field strength is reducing, flux density reduces in different ratio. As can be seen in Figure 1.14, after the magnetic field strength reaches zero, some magnetizations are remaining, that is called as Remanence or Residual Magnetization (M_r). That is, there is a magnetism in ferromagnetic or ferrimagnetic materials after the external magnetic field removed.

The magnetic field direction must direct completely opposite and has a certain magnitude for reduce the magnetization to zero. Coercivity or Coercive Force (H_c), show the resistance to demagnetization of materials. As can be seen in Figure 1.15, after the specimen pass the $-H_c$ point, reaches the oppositely directed magnetic saturation. That is, magnetic field direction of material is completely reversal, and it has same magnitude. After the materials reached oppositely directed magnetic saturation, direction of magnetic field is changed to opposite direction again. Residual magnetization and coercive force values are obtained as opposite directed with reversal process of magnetic field. There is a loop occurs due to reversal of the process and it calls hysteresis loop.

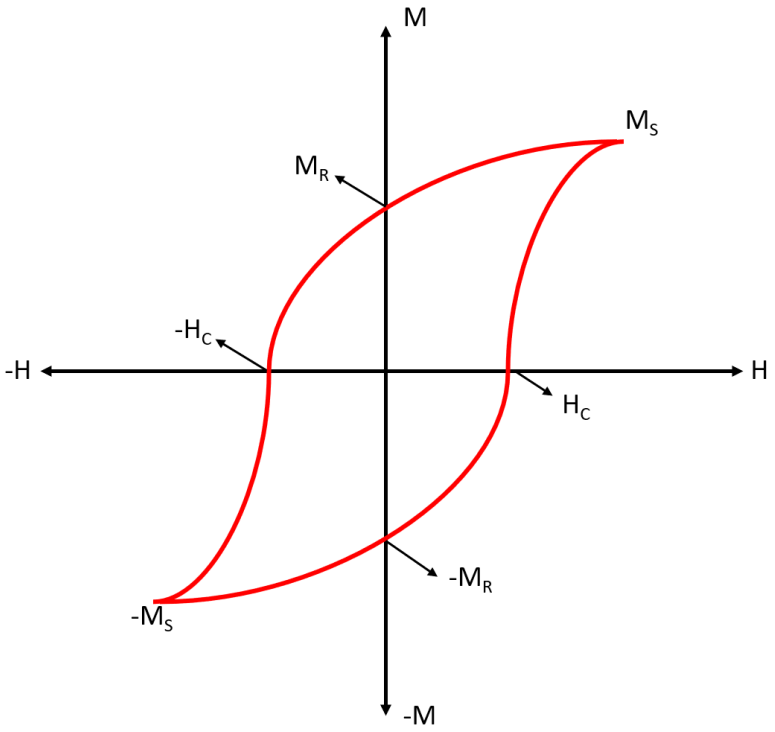

Figure 1.15: Representation of hysteresis loop graph.

1.3.1.11 Currie Temperature

Vibration of atoms is increased by rising the temperature and this conduce to magnetic moments of atoms can rotate freely [13]. Alignment of magnetic moments become randomize and this affects magnetic properties of materials. This critical temperature is called Curie Temperature (T_c). For instance, ferromagnetic materials exhibit paramagnetic properties above the Curie temperature [14]. Lower temperatures such as 0 K leads to highest saturation of magnetization due to minimum thermal vibration [13]. Antiferromagnetism is also affected by temperature. In contrast to Curie temperature, an antiferromagnetic material shows paramagnetic features above the Néel temperature [13].

1.3.2 Magnetic Materials

Magnetic materials have a wide range of application fields such as electronic, computing, electricity generation, or motion generation [13], [16]. Magnetic materials can be divided into two subgroups due to size and shapes of their hysteresis loops, soft and hard magnetic materials [14], [17]. As can be seen in Figure 1.15, soft magnetic materials have more narrow hysteresis loops and hard magnetic materials have more broad loops.

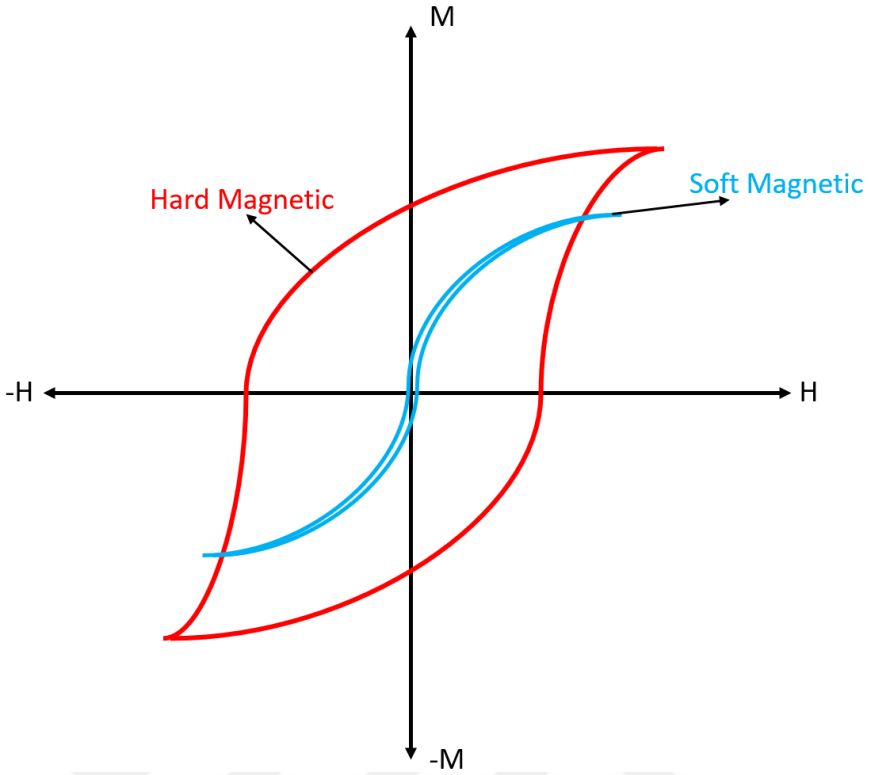

Figure 1.16: Representation of hysteresis loop of hard and soft magnetic materials.

1.3.2.1 Soft Magnetic Materials

Soft magnetic materials have more narrow hysteresis loops than hard magnetic materials [13], [14]. The soft magnetic materials can be easily magnetized and demagnetized, and they exhibit higher magnetic permeability. Soft magnets can strengthen to the magnetic fluxes are generated by electric current due to their features [17]. Energy generation, transformation, and transportation devices includes soft magnetic materials [13]. Soft magnetic materials are used in devices such as, electricity generator, transformer, and electric motors, because of soft magnetic materials have low energy losses as can be seen in Table 1.5 [13]. Silicon steels, Permaloy, Permendur, Hypernik, Mumetal, Supermalloy, Metglas, Finmet, etc. are examples of commercial soft magnetic alloys. Soft magnetic materials such as Silicon Steels (Fe-3% wt. Si) or Permoloy have become a standard materials for electricity generation, transmission, and sensors [18]. Conventional soft magnetic materials have numerous limitations, e.g., complex processing requirements and poor strength [19]. The worldwide market values of soft magnetic materials were $48 billion in 2018 and this market is expected to increase to $85 billion by 2026 [19]. Even a small improvement in the efficiency of electrical machines, which consume

more than 40% of global electricity production, can have a large impact on energy savings and reduce CO_2 emissions [19].

Table 1.5: Typical properties for several soft magnetic materials [13].

Materials	Composition (%w)	Initial Relative Permeability (μ_i)	Saturation Flux Density B_s [tesla (gauss)]	Hysteresis Loss/Cycle [J/m^3 (erg/cm^3)]
Commericail Iron Ingot	99.95 Fe	150	2.14 (21,400)	270 (2700)
Silicon-Iron (Oriented)	97 Fe, 3 Si	1400	2.01 (20,100)	40 (400)
45 Permaloy	55 Fe, 45 Ni	2500	1.60 (16,000)	120 (1200)
Supermaloy	79 Ni, 15 Fe, 5 Mo, 0.5 Mn	75,000	0.80 (8000)	–
Ferroxcube A	48 $MnFe_2O_4$, 52 $ZnFe_2O_4$	1400	0.33 (3300)	~40 (~400)
Ferroxcube B	36 $NiFe_2O_4$, 64 $ZnFe_2O_4$	650	0.36 (3600)	~35 (~350)

1.3.2.2 Hard Magnetic Materials

The hard magnetic materials have wider hysteresis loops than that of the soft magnetic materials. They have stronger coercive forces and higher residual magnetization [13], [15]. That is, once they are magnetized, demagnetization process will become tough for them. Hard magnetic materials are also known as Permanent Magnets (PM) duesto their long-term magnetism after the magnetization. Lodestone was the first permanent magnet [15]. Today, PMs are used in many different technological fields and in many different devices such as, loudspeakers, data storage, in brushless DC motors. PMs generates permanent magnetic field in a certain volume Due to this particular property of PMs, magnetic field is generated without using electricity [14]. Magnetic strength of PMs is calculated with maximum energy production. As can be seen in Figure 1.17, maximum energy production of PMs is the maximum area of the rectangular fit into second quadrant of hysteresis loop [13], [14], [16]. The production of smaller volume magnets is an important trend for the development of more efficient instruments [16].The requirements for producing a strong magnet with good magnetic properties can be listed as [16]:

- The maximum energy production
- Flux density (Br),
- Energy production,
- Resistance to demagnetization,

- Usable temperature range,
- Temperature-varying magnetization,
- Demagnetization curve (2nd quarter),
- Corrosion resistance,
- Mechanical strengths,
- Electrical resistance,
- The magnetic field needs to become magnetized,
- Raw material costs.

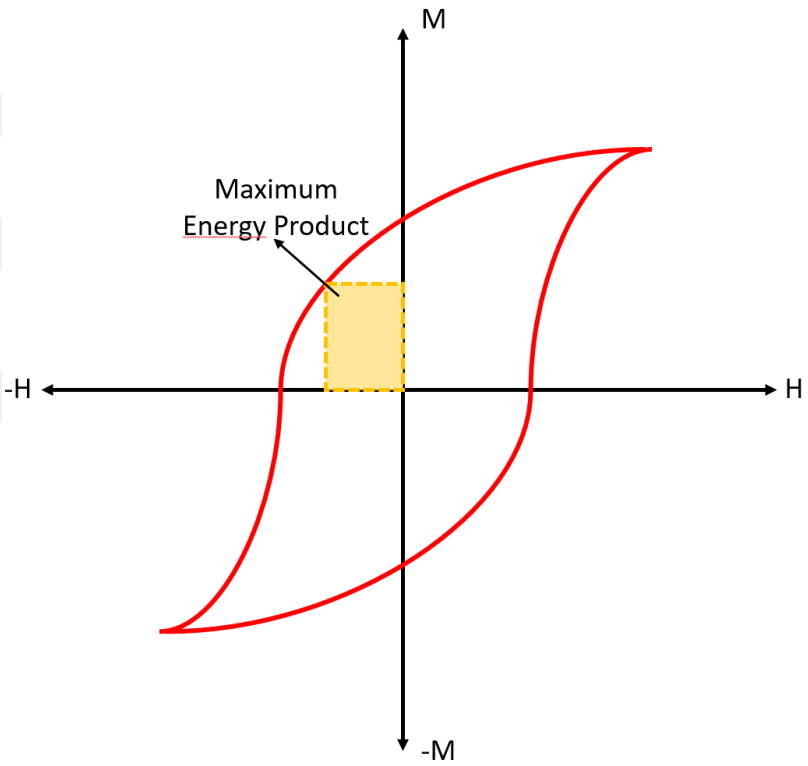

Figure 1.17: Representation of maximum energy product in B-H curve.

PMs were produced with Fe-based alloys until the 1900s. In the early 1900s, a new era has begun with the discovery of alnico magnets. High energy magnets were discovered in late 1900s [17]. The magnetic properties of commonly used magnets;Alnico, Sm-Co, and Nd-Fe-B, are tabulated in Table 1.6.

Table 1.6: Properties of hard magnetic materials [18].

Properties	**Alnico**	**$SmCo_5$**	**Sm_2Co_{17}**	**Nd-Fe-B**
BH_{max} (kJ/m^3)	7 ~ 80	119 ~ 160	159 ~ 264	199 ~ 444
B_r (T)	0.7 ~ 1.4	0.8 ~ 0.9	0.9 ~ 1.1	1.0 ~ 1.4
H_{ci} (kA/m)	39 ~ 239	≥ 1197	798 ~ 2400	798 ~ 2394
T_c (C°)	860	750	825	310
T_M (C°)	500	250	-0.30	100 ~ 250
Corrosion Resistance	Very Good	Good	Good	Poor

1.3.2.2.1 Alnico Magnets

Alnico magnets are one of the critical milestones for PMs. These magnets contain mainly Fe, Co, Ni, and Al elements and small amounts of Cu and Ti elements [15], [23]. The first alnico alloy was discovered by Mishima in 1931 [23]–[25]. Alnico magnets are cheaper than other magnet types such as Sm-Co and Nd-Fe-B because they don't contain any RE elements. Extraction and processing of RE elements are overcostly [24], [26]. In addition, alnico magnets have higher Currie Temperature [25]. After the discovery of high energy PMs in 1970s, the attention to the alnico magnets were critically decreased [25].

1.3.2.2.2 Sm-Co Magnets

In the last few decades, much attention were given to high energy PMs have i [18]. Achievement of higher magnetic properties at minimum volume is critical for advancing in technology. Different types of RE elements were studied to obtain strong RE-Co magnets [19]. Among all RE-Co magnets, the most attractive one is Sm-Co magnet. There are two different types of this magnetic alloy system; $SmCo_5$ and Sm_2Co_{17}. $SmCo_5$ magnets have very good magnetic characteristics such as high T_c value, high service temperature (T_M), and good corrosion resistance [18].

1.3.2.2.3 Nd-Fe-B Magnets

Since the innovation of RE and transition metal alloyed magnets, many studies have been done on them. After a decade from the discovery of Sm-Co magnets, Nd-Fe-B magnets were discovered in 1983 [20], [21]. Nd-Fe-B magnets have much better magnetic properties than others such as their higher maximum energy production value. Nd-Fe-B magnets can produce more magnetic field in smaller volume. Since their discovery Nd-Fe-B magnets have been used for many variety of industrial areas [13], [21], [22].

1.4 MAGNETIC HIGH ENTROPY ALLOYS

HEAs have attracted much attention due to their unique mechanical, thermal, physical, and electrical properties. Recent studies have shown that HEAs alloys have significant magnetic properties, as well. Due to technological developments, and the requirements for new magnetic material is increasing. Figure 1.18 indicates the number of sales of permanent magnets per years from 1980s to 2020s. It is obvious that the needs for magnetic materials are increasing year by year and for instance over $ 16 million sales were done in 2020. Today, most widely used strong magnets are rare earth (RE) based ones. Due to the presence of RE elements, the production cost of high energy magnets used widely in industry is extremely high. [23]. Therefore, it is significant to develop new magnetic materials, and much effort has been given to investigate magnetic properties of HEAs. Recent studies have indicated the magnetic properties of HEAs, and due to their attractive magnetic properties, these alloys were named as Magnetic High Entropy Alloys [24].

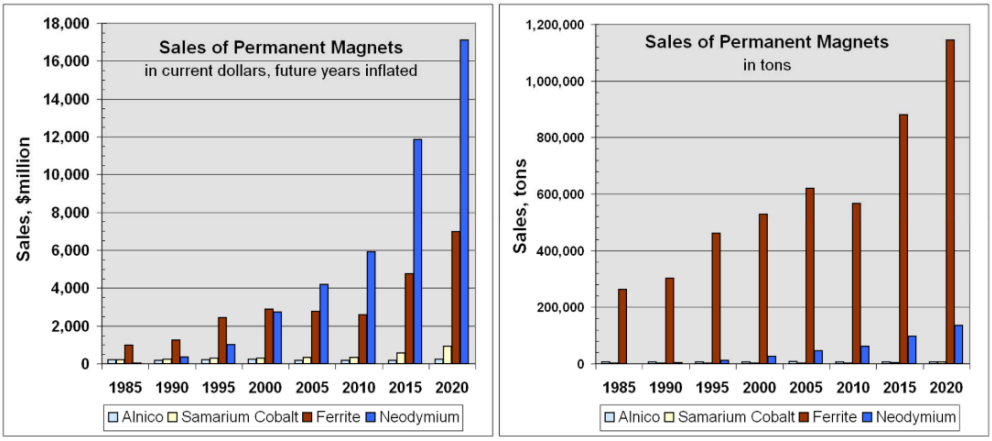

Figure 1.18: Permanent magnet sales by US Dollars and by metric tons for the four largest commercially available materials.

Magnetic alloys commonly have more than 50% at. of ferromagnetic elements, such as Fe, Co, and Ni [25]. Magnetic alloys consist of ferromagnetic transition metals such as FeCoNi usually show soft magnetic properties [26]. R. Kulkarni et al., investigated the effect of Fe and Cu on the magnetic properties of AlNiCo alloy. They reported that the addition of Cu increases both the coercivity (H_c) of the alloy from ~0 Oe to 650 Oe and the residual magnetism (B_r) from ~0 emu/g to 2.6 emu/g of AlNiCo alloy. Their study also showed that the addition of Fe alone increases the magnetic saturation (M_s) of the alloy to97 emu/g. It was also

mentioned that M_s, H_c, and M_r of AlNiCo alloy reached to 84 emu/g, 162 Oe, and 5.2 emu/g, respectively with the addition Cu and Fe[25].

Table 1.7: The effect of Cu and Fe on the magnetic properties of AlNiCo alloy [25].

ALLOY	M_s (EMU/G)	H_c (OE)	M_r (EMU/G)
ALNICO	NonSaturating	~0	~0
ALNiCOCU	5.9	650	2.3
ALNICOFE	97	~0	~0
ALNICOCUFE	84	162	5.3

T. Borkar et al. [27] reported that the increase in magnetic saturation of $AlFeNiCo_xCr_{1-x}$ alloy dramatically with the change of Co/Cr ratio. They stated that Co increases the Ms of the alloy from 18.48 emu/g to 117.8 emu/g. C. Liu et al. [28] investigated the magnetic properties of $AlCoCuFeNi_x$ alloy and reported that the increase in Ni decreases the Ms of the alloy from 89.21 emu/g to 54.69 emu/g while increases Hc of the alloy from 7.30 Oe to 24.81 Oe.V. Chaudhary et al. [24]., reported that the formation of BCC phase in $FeCoNiAl_xCr$ and $FeNiCoAl_x$ alloys increases M_s and Currie temperatures (T_c)values that of FCC phase. [24]. It has been reported that BCC phase improves the magnetic properties of the alloys. C. Zhao et al. stated that Ms of BCC phase is higher than that of the FCC phase [29]. Some of the elements facilitates the formation of BCC phase which improves magnetic properties of the alloys significantly. J. He et al. investigated the Al addition effect on the formation of BCC phase in $(FeCoCrMnNi)_{100-x}Al_x$ alloy, as seen in Figure 1.18. They concluded that when the Al concentration is less than 8 %at FCC phase forms while when the Al concentration is between 8 % at and 16 %at, BCC forms and when the Al concentration is higher than 16 % at. B2 (ordered BCC) phase forms [30]. W. Wang et al. showed the trigger effect of Al for the BCC formation in AlxCoCrFeNi alloy [31]. J. Cieslak et al. observed that M_s and T_c values increase as the Al content increases in the $Al_xFeCoCrNi$ alloy [32].

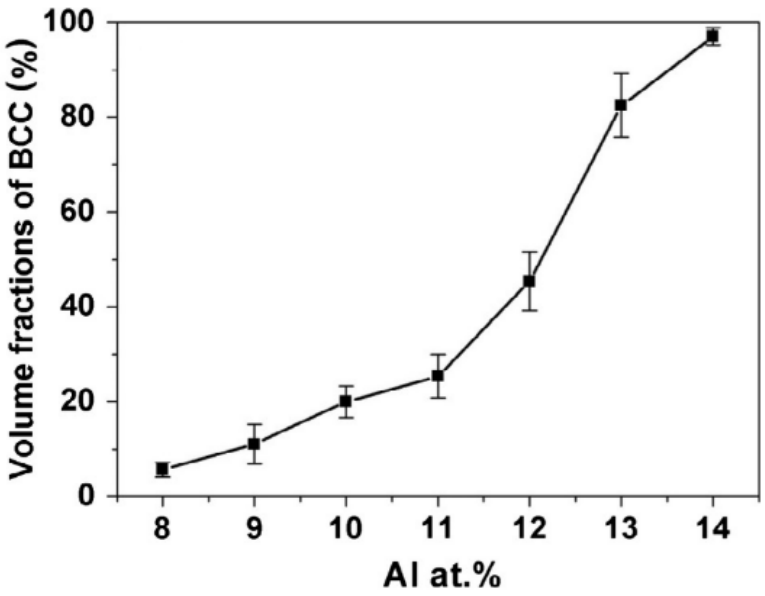

Figure 1.19: The effect of Al on the volume fraction of BCC in (FeCoCrMnNi)100-xAlx alloy [30].

R. Mishra et al. [33] investigated the magnetic properties of as-cast and isothermally annealed AlCrFeMnNiTi alloy. They reported that the as-cast alloy indicates good soft magnetic properties, and the magnetization decreases after annealing due to the change in the amount of the magnetic phase and the distribution of the magnetic elements. They also stated that the annealed alloy shows better corrosion resistance due to the formation of protective layer on the surface [33]. Wu et al. [34] investigated the addition of very low amounts of Ce on the corrosive and magnetic properties of the FeCoNiCuAl alloy. They reported that magnetic properties of $FeCoNiCuAlCe_x$ (x = 0 - 0.09) alloy enhance most when the x=0.09. It was also mentioned that the corrosion resistance of the alloy is increasing with Ce, even it is better that that of 304 stainless steels. They also suggested that the Ce addition improves the high temperature stability of the alloy.

CHAPTER II

2. EXPERIMENTAL PROCEDURE

2.1 ALLOY PRODUCTION

The alloys were designed based on thermodynamic calculations and Hume-Rothery rules. The alloy ingots were synthesized from high purity elements (0.999 Al, Co, Cu, Fe, Ni, Nb, Ti and V, by weight) under an Ar atmosphere using Compact Arc Melter MAM-1 produced by Edmund Bühler with turbo-molecular pump, given in Figure 2.1. To achieve chemical homogeneity, the alloys were remelted at least 3 times.

Figure 2.1: Edmund Bühler Compact Arc Melter MAM-1

2.2 HEAT TREATMENT

The heat treatment processes of as-cast alloys were performed to investigate the temperature stability of their magnetic properties. The heat treatment of as-cast alloys was done using Protherm Furnaces P1 115M heat, indicated in Figure 2.2. The as-cast alloys were inserted into the furnace when the temperature is reached to 928 K (675 C) and isothermally annealed at 928 K (675 C) for 3 hours and 24 hours and then cooled in furnace.

Figure 2.2: Protherm Furnaces P1 115M heat treatment furnace.

2.3 CHARACTERICATION TECHNIQUES

The as-cast and heat-treated alloys were investigated using several characterization techniques such as X-Ray diffraction (XRD), optical microscope (OM), scanning electron microscope (SEM), vibrating sample magnetometer (VSM), and hardness testing. XRD and VSM techniques were performed on the powder form of alloys. Thus, ball milling was used to produce powders of the alloys using SPEX SamplePrep 8000M Mixer/Mill ball milling device, given in Figure 2.3.

Figure 2.3:SPEX SamplePrep 8000M Mixer/Mill ball milling device.

2.3.1 X-Ray Draffraction Analysis

The structure and phase stability of the as-cast and heat-treated alloys were investigated by XRD analysis using Rigaku XRD device. XRD is a non-destructive analysis technique that gives the quantitative properties, phase composition, crystal structure, and texture of the material [35]–[37]. The diffraction data were collected with a diffraction angle ranging from 10° to 100° with a scanning rate of 2°/min. XRD analysis were performed on the powdered alloys.

2.3.2 Optical Microscope and Scanning Electron Microscope

The microstructural characterization of as-cast and heat-treated alloys were performed using OM and SEM analysis. The surface morphology, distribution of phases, shape, and structure of the samples were examined by microstructural analysis using Nikon Eclipse LV150 optical microscope, in Figure 2.4 (a). The specimens were initially metallographically prepared before the OM and SEM investigations. The samples were ground with 180, 240, 320, 400, 600, 800, 1000, 1200, 2000, and 2500 grit size SiC papers and then, 0.3 mm Alumina solution was used for polishing. The samples etched with aqua regia solution (3HCl:HNO_3).

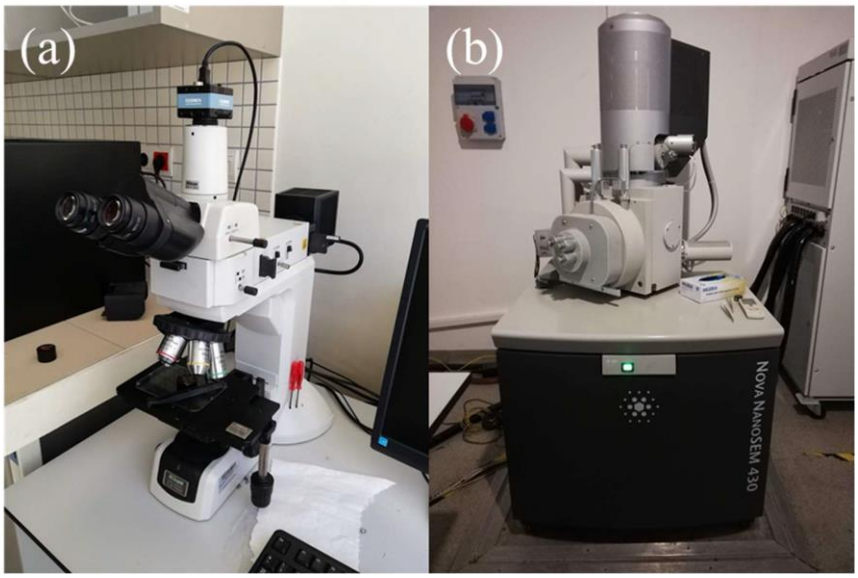

Figure 2.4:(a) Nikon Eclipse LV150 optical microscope. (b) FEI Nova NanoSEM 430 Scanning electron microscope.

The SEM analysis was done using FEI Nova NanoSEM 430 Scanning electron microscope. The elemental analysis was achieved using Energy-dispersive

X-ray Spectroscopy detector (EDS) inserted in FEI Nova NanoSEM 430 scanning electron microscope. The line scanning EDS data collection was also used.

2.3.3 Magnetic Tests

The magnetic properties of the as-cast and heat-treated alloys were determined using VSM. Hysteresis curve obtained from VSM analysis gives much information about magnetic properties of sample such as magnetic saturation, coercive force, and residual magnetization. Also, the magnetic properties of the materials, such as whether they are ferromagnetic or ferrimagnetic; even information about whether they are hard or soft magnets can be accessed through this test[38]. The VSM magnetic movement is a precision measuring device that works as a function of the magnetic field [39].

VSM analyzes were carried out using Cryogenic Limited PPMS test device, given in Figure 2.6, at Central Laboratory, Middle East Technical University (METU). VSM measurements were performed at room temperature.

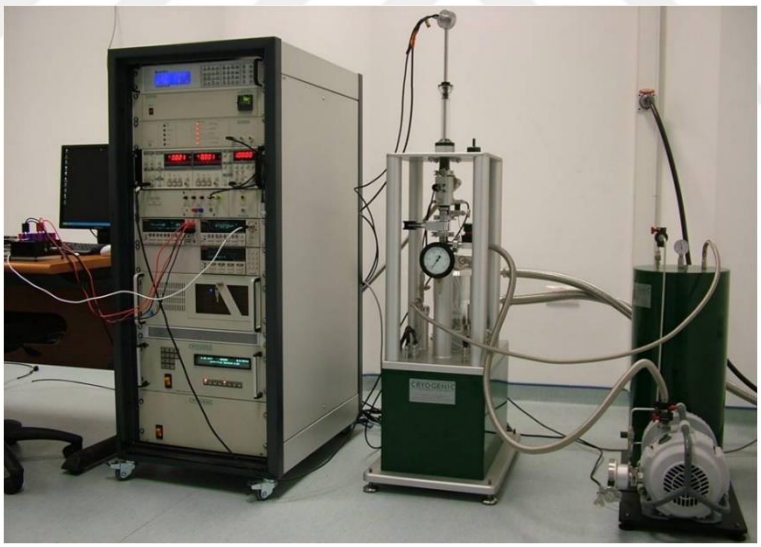

Figure 2.5: Cryogenic Limited PPMS at Central Laboratory, METU.

2.3.4 Hardness Test

The hardness measurements of the as-cast and heat-treated alloys were carried out using INNOVATEST Nexus 7500TM Universal Hardness Tester, shown in Figure 2.6. The specimens were prepared metallographically before the application of hardness tests. Surfaces of samples were grinded, polished, and etched with aqua regia before analysis The Vickers Hardness (HV) tests were performed

due to ASTM Standard E92, and ASTM Standard E384 [13].At least 10 measurements were taken from the samples to calculate the average hardness values and the standard deviations.

Figure 2.6:INNOVATEST Nexus 7500TM Universal Hardness Tester.

CHAPTER III

3. RESULTS AND DISCUSSION

3.1 ALLOY DESIGN

The alloys were designed based on the thermodynamic parameters, calculated using the relationships (equations 1-6) given in previous sections. The atomic parameters, structural and magnetic properties of constituent elements of the alloys are given in Table 3.1. These are the critical properties for the determination of solid solution formation. Table 3.2 indicates the alloy compositions of the alloys the ferromagnetic Fe, Ni, and Co elements were used in all alloys. V and Nb were used to replace Ti. The calculated physical and thermodynamic parameters, such as atomic size difference (δ), ΔX, VEC, ΔSconf and ΔHmix of of $Fe_2CoNiAlCu_{0.4}Ti_{0.4}$, $Fe_2Co_{1.5}NiAlCu_{0.4}Ti_{0.4}$, $Fe_2Co_{1.5}NiAlCu_{0.5}Ti_{0.5}$, $FeCoNiAlCu$, $FeCoNiAlCu_{0.5}V_{0.5}$ and $FeCoNiAlCu_{0.5}Nb_{0.5}$ were given in Table 3.3. The thermodynamic and physical properties change with the variation of constituent elements. It is clear that each alloy has an atomic radii difference lower than 15%. Fe_2, $Fe_2Co_{1.5}$, and $Cu_{0.5}Ti_{0.5}$ alloys have the values of VEC between 6.8 and 8.0 which suggests BCC+FCC dual phase formation.

Table 3.1: Atomic, structural, and magnetic properties of constituent elements.

Elements	Atomic Radii (nm)	Electronegativity	Valance Electron	Crystal Structure	Magnetism Type
Al	0.143	1.61	3	FCC	Paramagnetic
Ti	0.147	1.54	4	HCP	Paramagnetic
V	0.134	1.63	5	BCC	-
Fe	0.126	1.83	8	BCC	Ferromagnetic
Co	0.125	1.88	9	HCP	Ferromagnetic
Ni	0.124	1.91	10	FCC	Ferromagnetic
Cu	0.128	1.9	11	FCC	Diamagnetic
Nb	0.146	1.6	5	BCC	-

Table 3.2: The compositions of designed alloys in weight percentage.

Formula	Al	Ti	V	Fe	Co	Ni	Cu	Nb
$Fe_2CoNiAlCu_{0.4}Ti_{0.4}$	17.24	6.90	-	34.48	17.24	17.24	6.90	-
$Fe_2Co_{1.5}NiAlCu_{0.4}Ti_{0.4}$	15.87	6.35	-	31.75	23.81	15.87	6.35	-
$Fe_2Co_{1.5}NiAlCu_{0.5}Ti_{0.5}$	15.38	7.69	-	30.77	23.08	15.38	7.69	-
FeCoNiAlCu	20	-	-	20	20	20	20	-
$FeCoNiAlCu_{0.5}V_{0.5}$	20	-	10	20	20	20	10	-
$FeCoNiAlCu_{0.5}Nb_{0.5}$	20	-	-	20	20	20	10	10

Table 3.3: The physical and thermodynamic parameters of alloys.

Formula	δ (%)	ΔX	VEC	ΔS_{conf}	ΔH_{mix}
$Fe_2CoNiAlCu_{0.4}Ti_{0.4}$	14.7079	0.6428	7.59	-13.678	-15.5677
$Fe_2Co_{1.5}NiAlCu_{0.4}Ti_{0.4}$	14.7517	0.5932	7.70	-13.638	-14.9624
$Fe_2Co_{1.5}NiAlCu_{0.5}Ti_{0.5}$	14.7272	0.5765	7.69	-13.898	-15.7657
FeCoNiAlCu	11.3003	0.3826	8.20	-13.381	-12.0160
$FeCoNiAlCu_{0.5}V_{0.5}$	13.8675	0.3859	7.60	-14.533	-14.6080
$FeCoNiAlCu_{0.5}Nb_{0.5}$	14.6565	0.3873	7.60	-14.533	-17.3360

Table 3.4: Alloy codes and the corresponding conditions.

Formula	Alloy code	Condition
$Fe_2CoNiAlCu_{0.4}Ti_{0.4}$	M-01	As-cast
	M-01-3HT	3 hours Heat Treated at 948 K
	M-01-24HT	24 hours Heat Treated at 948 K
$Fe_2Co_{1.5}NiAlCu_{0.4}Ti_{0.4}$	M-02	As-cast
	M-02-3HT	3 hours Heat Treated at 948 K
	M-02-24HT	24 hours Heat Treated at 948 K
$Fe_2Co_{1.5}NiAlCu_{0.5}Ti_{0.5}$	M-03	As-cast
	M-03-3HT	3 hours Heat Treated at 948 K
	M-03-24HT	24 hours Heat Treated at 948 K
FeCoNiAlCu	M-11	As-cast
$FeCoNiAlCu_{0.5}V_{0.5}$	M-12	As-cast
$FeCoNiAlCu_{0.5}Nb_{0.5}$	M-13	As-cast

3.2 CHARACTERIZATION OF HIGH ENTROPY ALLOYS

Figure 3.1 illustrates the XRD patterns of as-cast $Fe_2CoNiAlCu_{0.4}Ti_{0.4}$ (M-01), $Fe_2Co_{1.5}NiAlCu_{0.4}Ti_{0.4}$ (M-02) and $Fe_2Co_{1.5}NiAlCu_{0.5}Ti_{0.5}$ (M-03) alloys. XRD analysis shows the single BCC phase structure for all these three alloys which is not

consistent with VEC calculations suggesting dual BCC+FCC structure. It shows that VEC is not enough parameter to show the crystal structures of the HEAs. The lattice parameters of BCC phase were determined as are 2.87711, 2.87536, and 2.87526 nm for M-01, M-02, and M-03, respectively. The lattice parameters of M-02 and M-03 are much closer to each other as their compositions are closer to each other compared to M-01.

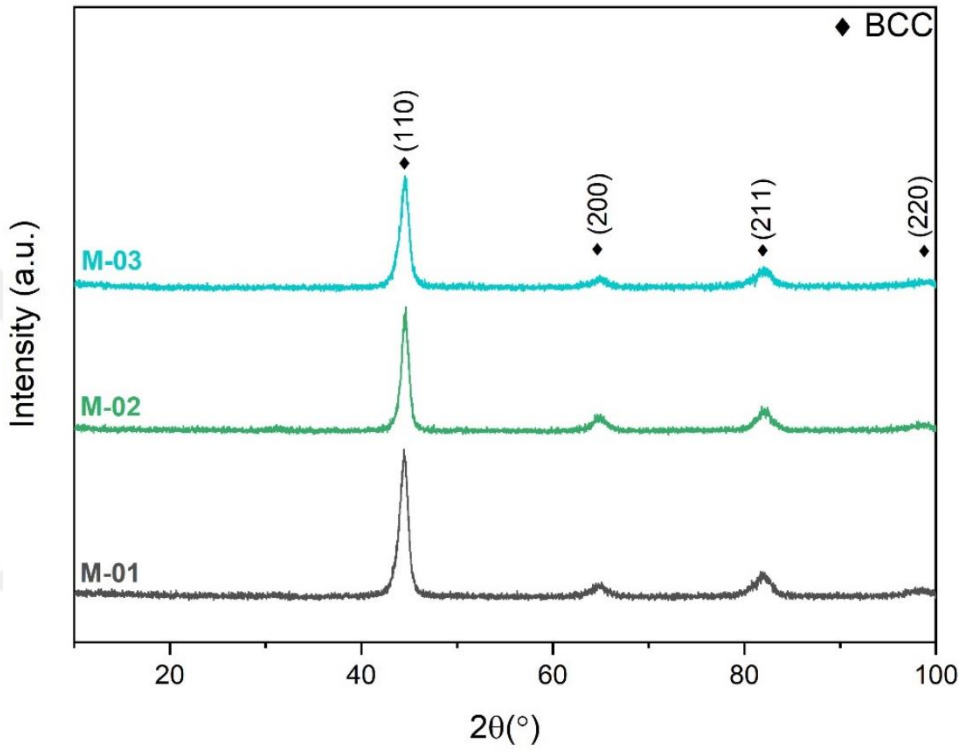

Figure 3.1:XRD patterns of M-01, M-02, and M-03.

The microstructure analysis of HEAs were first carried out with optical microscope (OM). The OM images of M-01, M-02 and M-03 alloys are shown in Figure 3.2 (a, b), (c, d) and (e. f), respectively. The OM images confirm the single-phase structure of M-01, M-02 and M-03 alloys. Equiaxed grain morphology of alloys can be seen from the images. the average grain size determination was done from the OM images. The average grain sizes of M-01, M-02 and M-03 alloys were measured as 29.48, 57.04, and 17.27 mm, respectively. The equiaxed grains of M-02 are larger than that of M-01 and M-03 alloys.

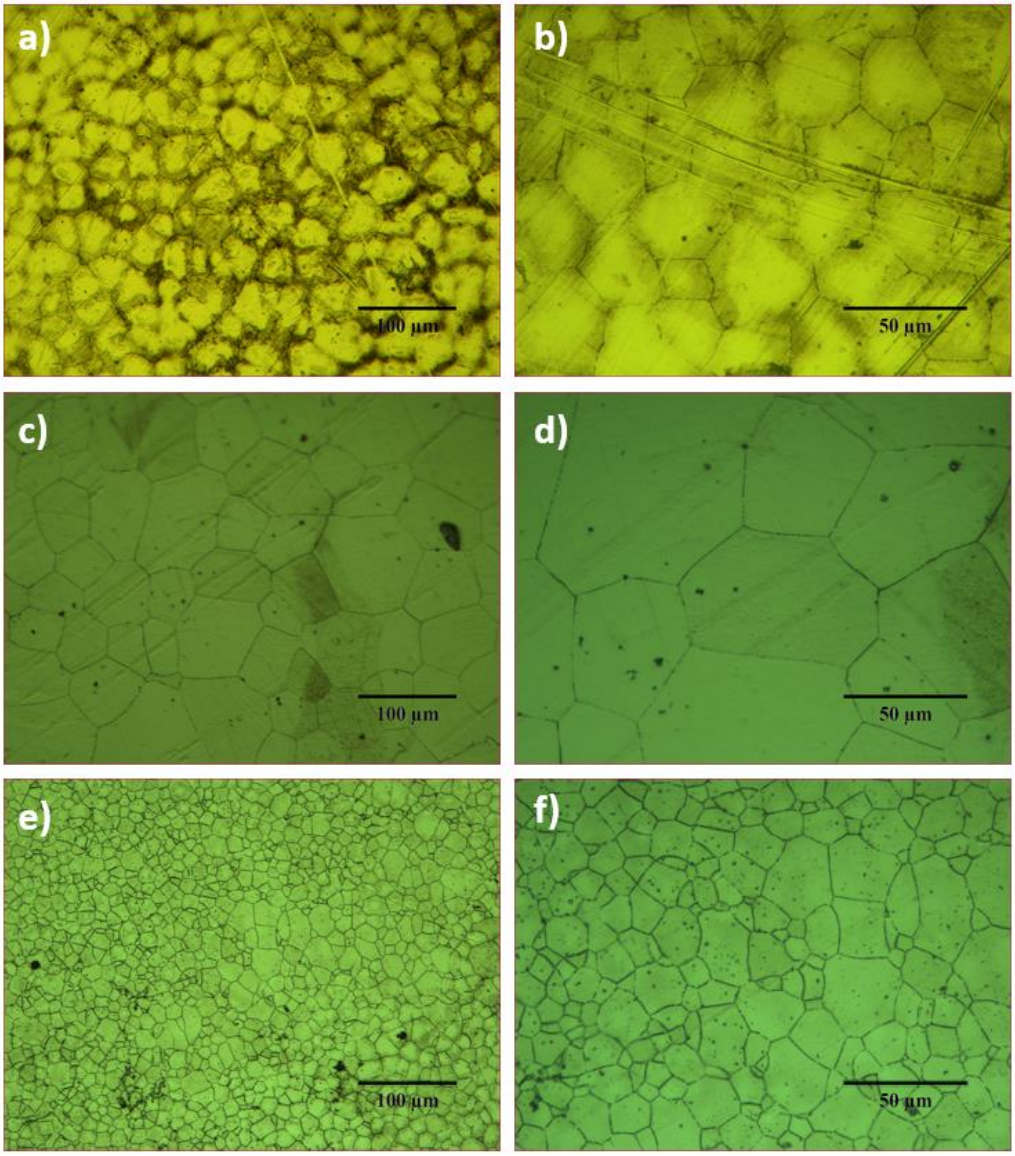

Figure 3.2:OM images of (a, b) M-01, (c-, d) M-02 (c, d), and (e, f) M-03 HEAs.

The thermal phase stability of M-01, M-02 and M-03 HEAs was investigated using XRD and OM. Figure 3.3 illustrates the XRD patterns of isothermally annealed M-01 alloy at 928 K for 3 and 24 hours in comparison to as-cast condition. It was observed that the single BCC phase structure of as-cast M-01 alloy does not change after 3 h heat treatment. The lattice parameter of M01-3HT alloy was calculated as 2.87299 nm, that shows the decrease in the lattice parameter of M-01 HEA alloy with annealing at 928 K for 3h. The XRD of isothermally annealed M-01 HEA at 928 K for 24 hours shows the formation of two new phases; $AlFe_3$ and $(Al_{0.5}Ti_{0.5})Ni_3$ phases with BCC. The structure of M-01 alloy has changed from single BCC to multi-phase.

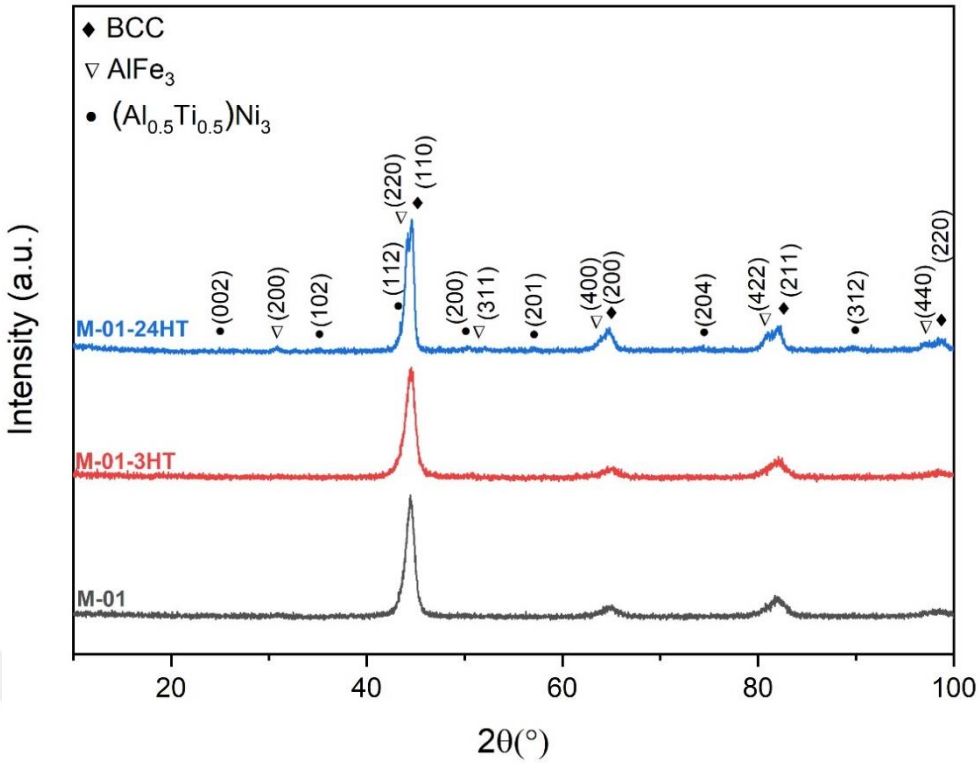

Figure 3.3:XRD patterns of M-01, M-01-3HT, and M-01-24HT.

The OM images of M-01, M-01-3HT, and M-01-24HT are illustrated in Figure 3.3 (a, b), (c, d) and (e, f) respectively. M-01 and M-01-3HT alloys exhibit single phase structure with similar equiaxed morphology. The increase in grain size was observed after 3h annealing of M-01 alloy. The grain size increases from 29.48 µm for as-cast M-01 to 35.45 µm for M-01-3HT alloy. The OM, in Figure 3.4, shows the formation of second phase for M-01-24HT alloy. The second phase sites at the grain boundaries of M-01-24HT alloy. The elemental distribution analysis of HEAs was done using EDS. Table 3.5 indicates the calculated values in comparison to analyzed values from EDS values of the elemental distribution of M-01 HEAs. The calculated average grain sizes of M-01, M-01-3HT, and M-01-24HT HEAs are summarized in Table 3.10.

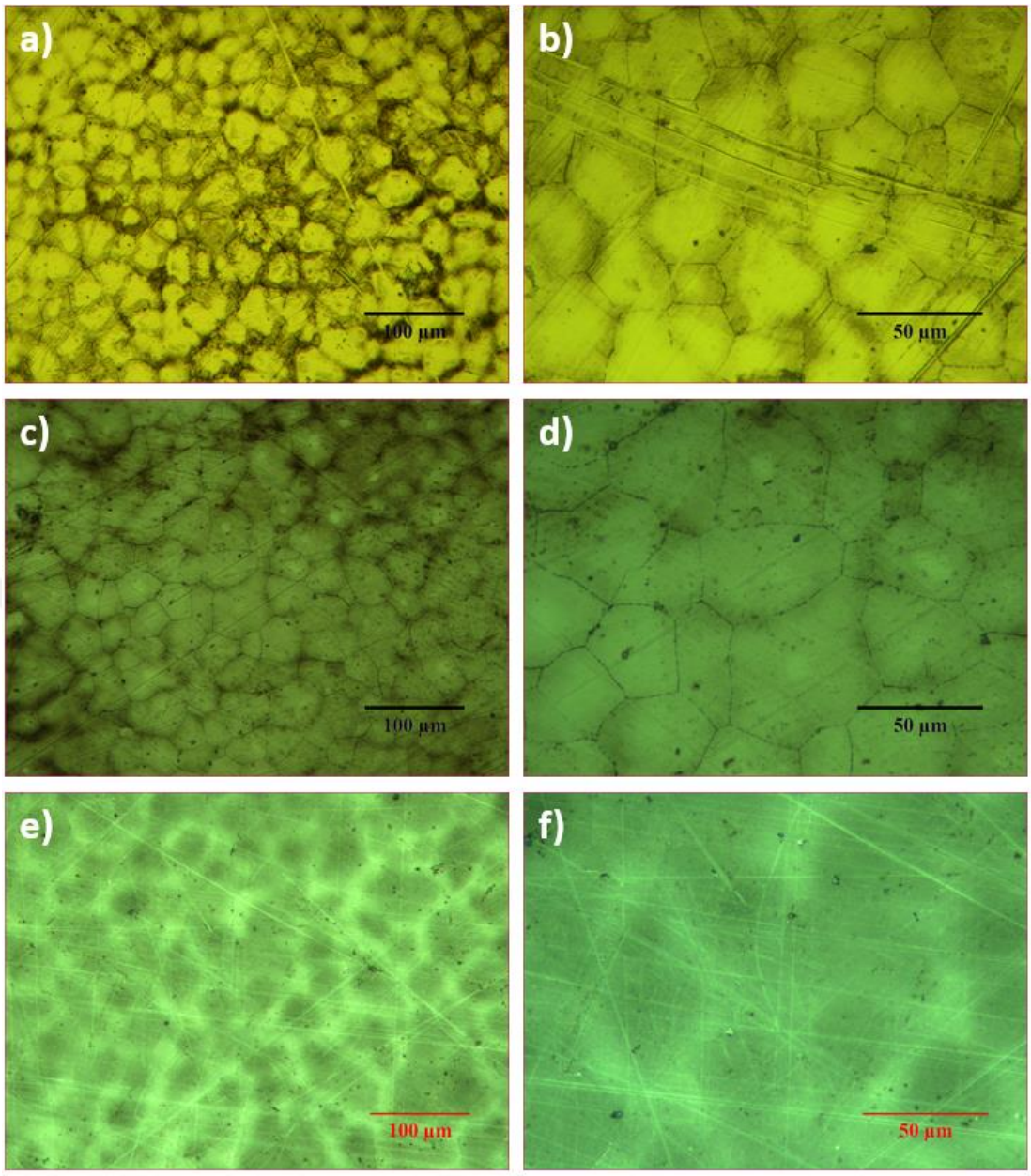

Figure 3.4: OM images of (a,b) M-01, (c,d) M-01-3HT, and (e, f) M-01-24HT.

Figure 3.5 illustrates the XRD patterns of isothermally annealed M-02 alloy at 928 K for 3 and 24 hours in comparison to as-cast condition. It is seen that the single BCC phase structure of as-cast M-02 alloy does not change after 3 h heat treatment. The lattice parameter of M02-3HT alloy was calculated as 2.86535 nm, that shows the decrease in the lattice parameter of M-02 HEA alloy with annealing at 928 K for 3h. The XRD of isothermally annealed M-02 HEA at 928 K for 24 hours shows the formation of two new phases; $AlFe_3$ and $(Al_{0.5}Ti_{0.5})Ni_3$ phases with BCC. The structure of M-02 alloy has changed from single BCC to multi-phase after isothermally annealed for 24 hours.

Table 3.5: Elemental distribution of M-01 HEA.

Elements	**Al**	**Ti**	**Fe**	**Co**	**Ni**	**Cu**
Calculated (% at.)	15.87	6.35	34.48	17.24	17.24	6.90
Analyzed (% at.)	14.94	7.34	35.47	17.36	17.90	6.99

The OM images of M-02, M-02-3HT, and M-02-24HT are shown in Figure 3.6 (a, b), (c, d), and (e, f) respectively. M-02 and M-02-3HT alloys exhibit single phase structure with equiaxed grain morphology similar to M-01 and M-01-3HT alloys. In contrast to M-01-3HT alloy, the decrease in grain size of M-02-3HT was observed after 3 hours annealing. The grain sizes of M-02 and M-02-3HT are calculated as 57.04 μm and 29,49 μm respectively. The OM images in Figure 3.6 (e, f), shows the second phase formation for M-02-24HT alloy. The second phase segregates along grain boundaries of M-02-24HT alloy. In addition to form new phases, surface morphology of M-02-24HT alloy transformed from the equiaxed grains to dendritic structure. Table 3.6 shows the calculated elemental values in comparison to elemental distribution achieved from EDS analysis of M-02 HEAs. The calculated average grain sizes of M-02, M-02-3HT, and M-02-24HT HEAs are summarized in Table 3.10, as well.

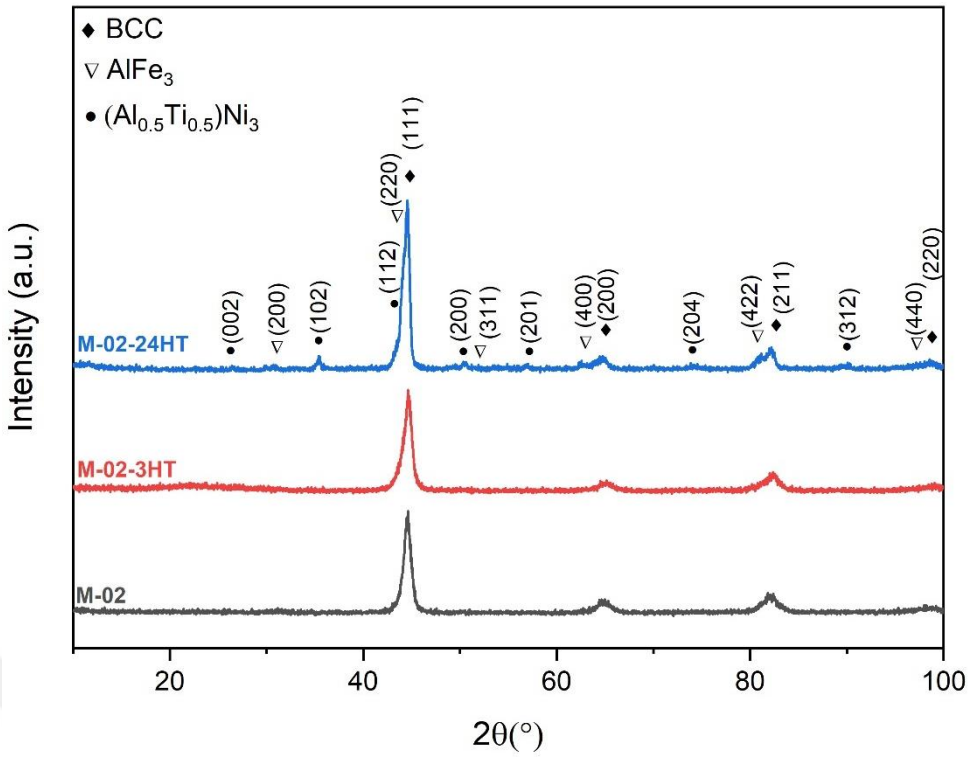

Figure 3.5:XRD patterns of M-02, M-02-3HT, and M-02-24HT.

Table 3.6: Elemental distribution of M-02.

Elements	**Al**	**Ti**	**Fe**	**Co**	**Ni**	**Cu**
Calculated (% at.)	15.87	6.35	31.75	23.81	15.87	6.35
Analyzed (% at.)	14.89	7.10	31.40	22.98	16.95	6.67

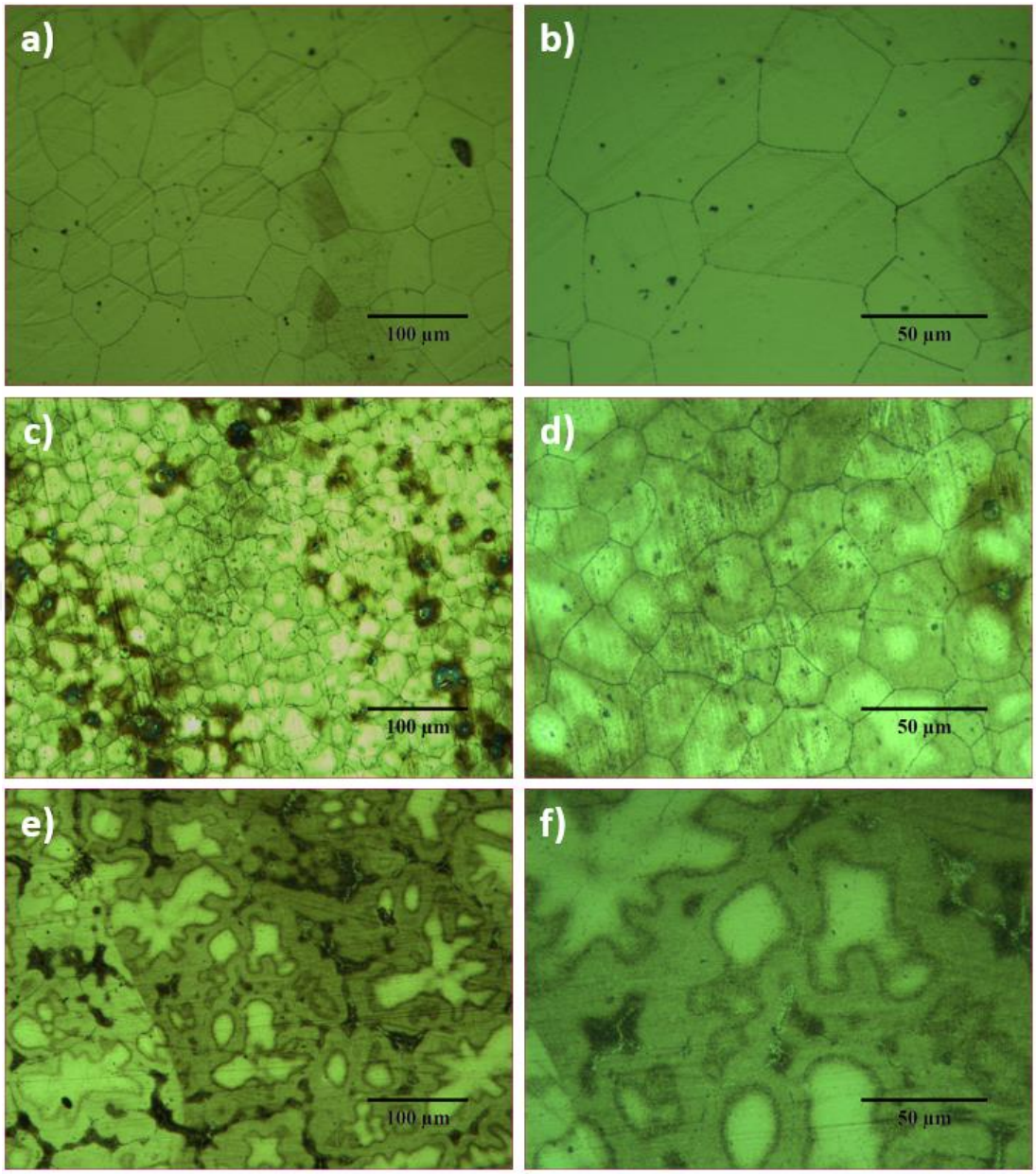

Figure 3.6:OM images of (a and b) M-02, (c and d) M-02-3HT, and (e and f) M-02-24HT.

Figure 3.6 illustrates the XRD patterns of isothermally annealed M-03 alloy at 928 K for 3 and 24 hours in comparison to as-cast condition. It was observed that the single BCC phase structure of as-cast M-03 alloy does not change after 3 h heat treatment. The lattice parameter of M-03-3HT alloy was calculated as 2.86535 nm. The lattice parameter of as-cast M-03 alloy decreases with annealing at 928 K for 3h. The XRD of isothermally annealed M-03 HEA at 928 K for 24 hours shows the formation of two new phases; $AlFe_3$ and $(Al_{0.5}Ti_{0.5})Ni_3$ phases with BCC similar to M-01-24HT and M-02-24HT.

Figure 3.8 (a, b), (c, d), and (e, f) shows the OM images of M-03, M-03-3HT, and M-03-24HT, respectively. M-03 and M-03-3HT alloys exhibit single phase structure with equiaxed grain morphology similar to M-01 alloys and M-02 alloys. The minimal increase in grain size of M-03-24HT was observed. The grain sizes of M-03 and M-03-3HT are 17.27 µm and 20.77 µm respectively. The OM images in Figure 3.8 (e, f), shows the formation of second phase for M-03-24HT. It is observed that second phase prefers to site through the grain boundaries of M-03-24HT alloy that is similar to that of M-01-24HT and M-02-24HT alloys. The morphological transition, from equiaxed grains to dendritic structure, is observed for M-03-24HT.

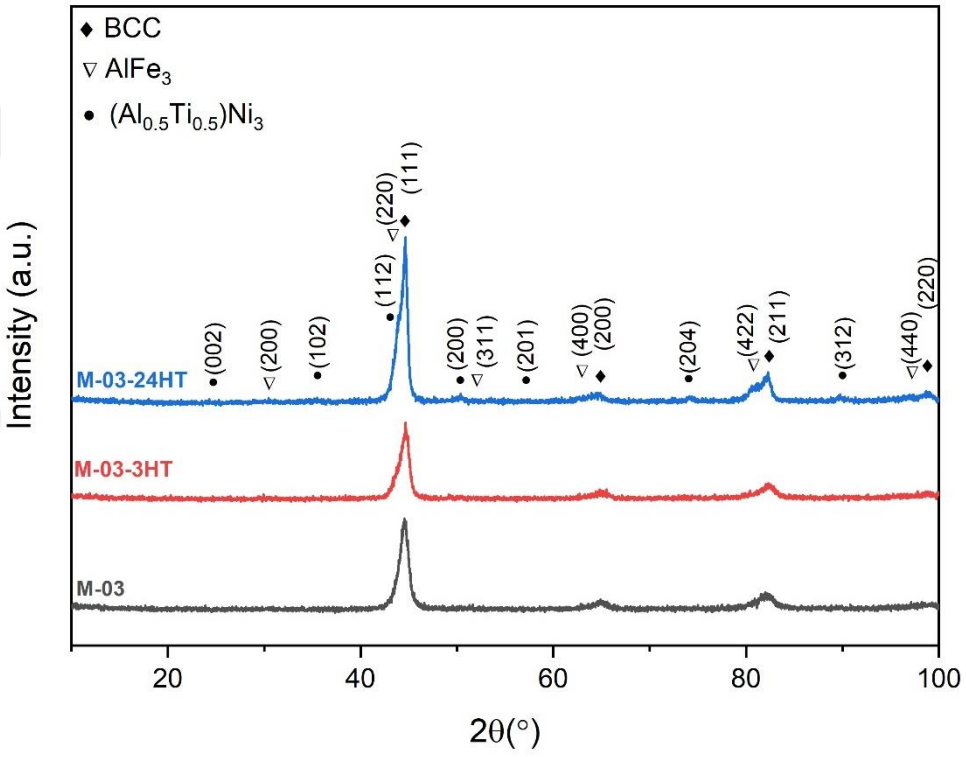

Figure 3.7: XRD patterns of M-03, M-03-3HT, and M-03-24HT alloys.

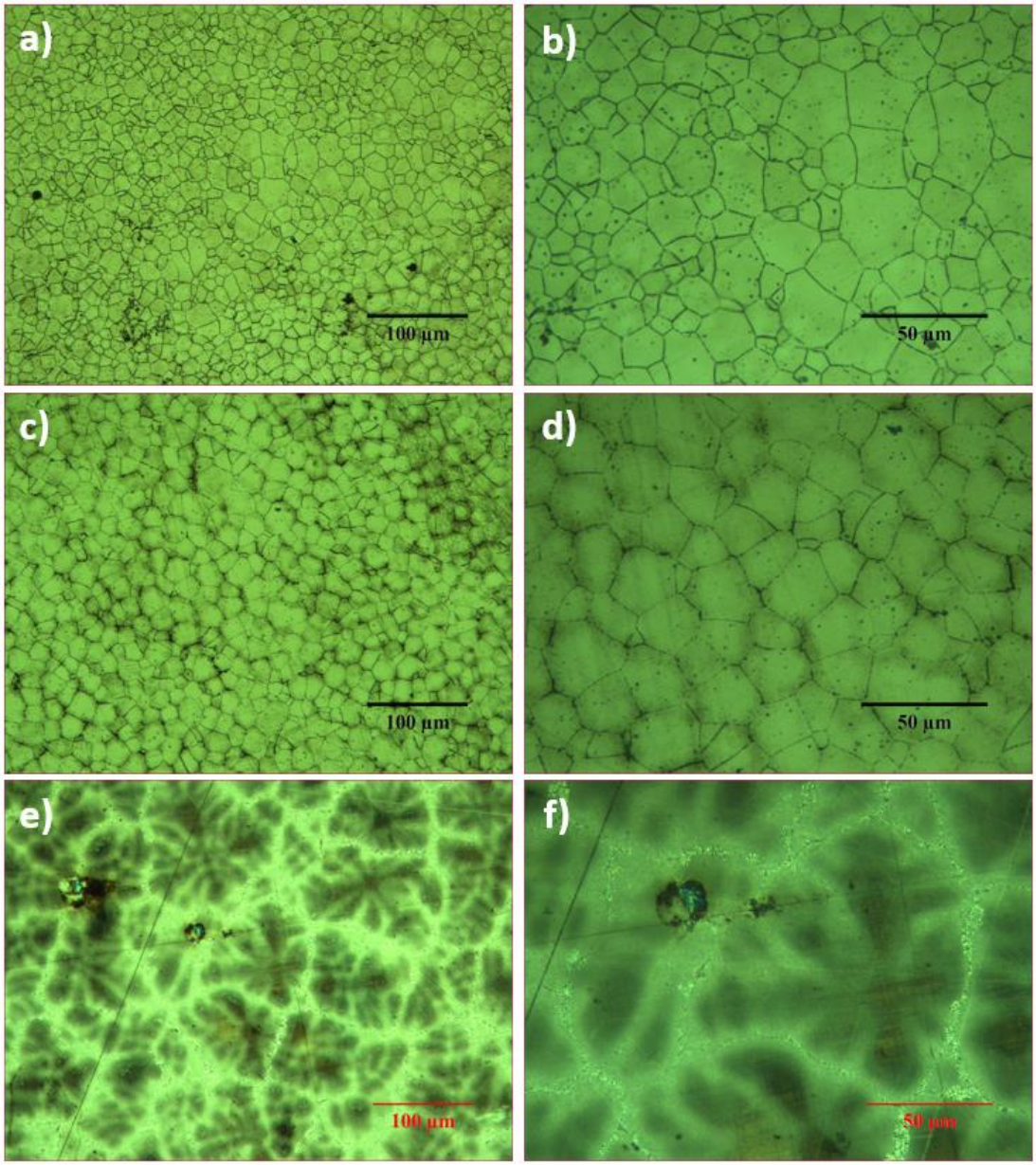

Figure 3.8:OM images of (a and b) M-03, (c and d) M-03-3HT, and (e and f) M-03-24HT alloys

Figure 3.9 illustrates the XRD pattern of M-11. XRD analysis indicates dual-phase structure of BCC+FCC. The lattice parameters of BCC and FCC phases were calculated as 2.87517 nm and 3.61587 nm respectively.

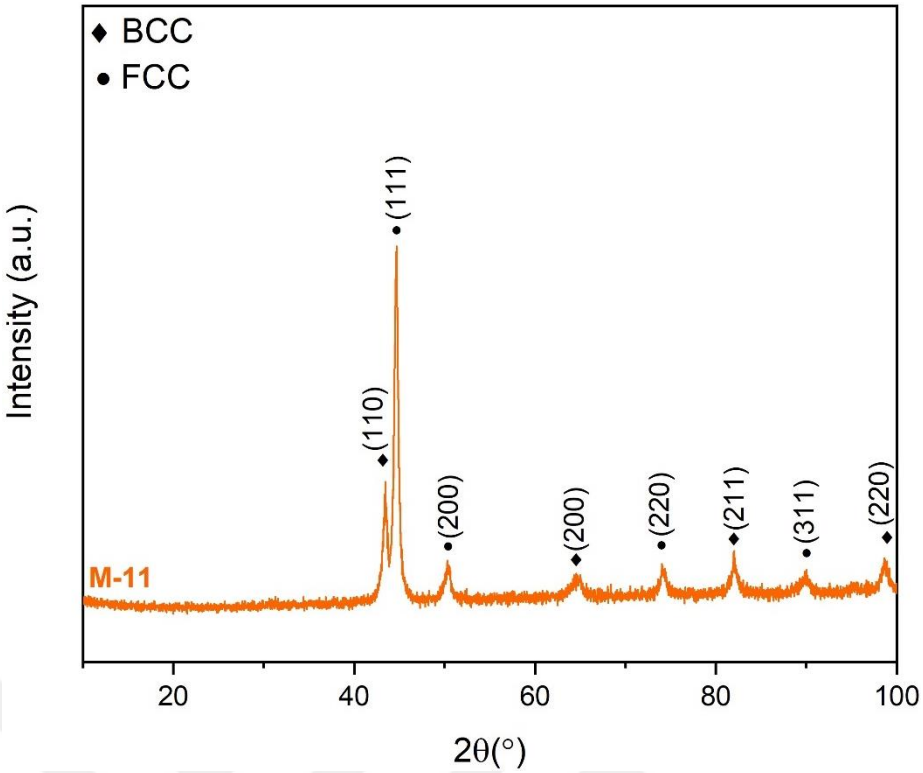

Figure 3.9: The XRD pattern of M-11 alloy.

Figure 3.10 (a, b, c, and d) shows the SEM images of M-11 alloy. SEM images confirm the XRD analysis as they exhibit two phases structure; in the form of lighter and darker regions. The elemental distribution analysis of M-11 was performed using line scanning EDS for more precise analysis. The direction and region of line and collected data are presented in Figure 3.11 (a) and (b) respectively. The increase in Al ratio and decrease in Cu ratio from dark region to light region o were observed. The lighter regions, which are rich by Al, possess the BCC structure due to lower VEC. The darker regions, which are rich by Cu, possess the FCC structure due to higher VEC.

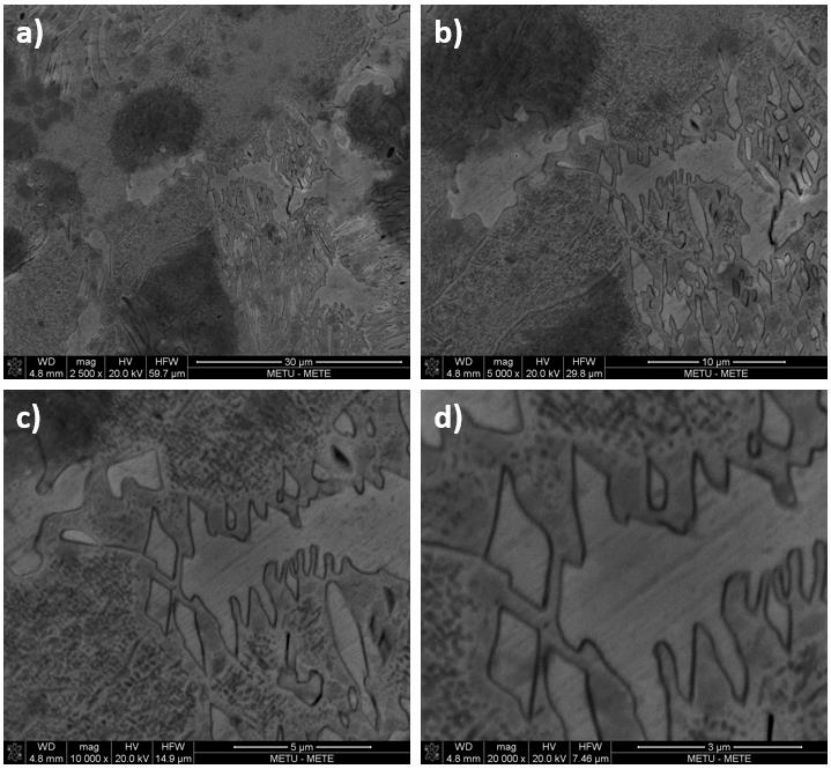

Figure 3.10:SEM images of M-11. (a) 2500x, (b) 5000x, (c) 10,000x, and (d) 20,000x are magnifications.

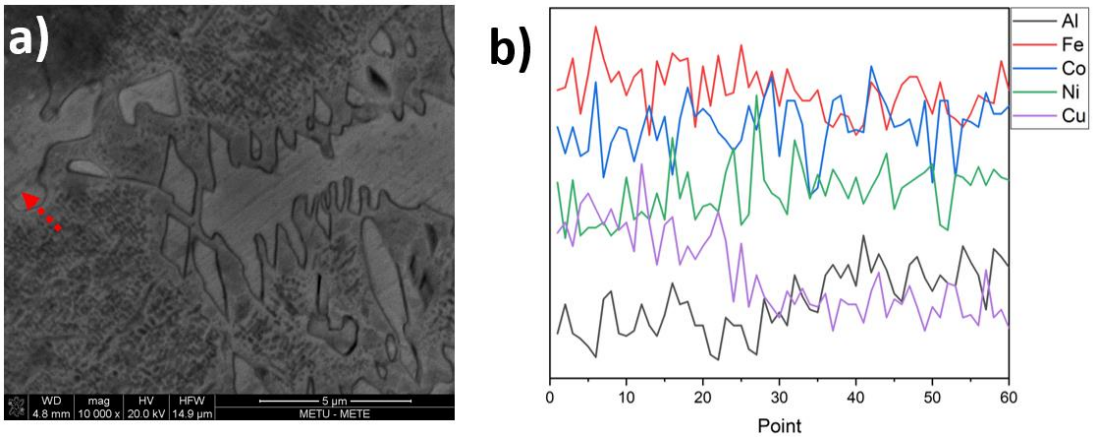

Figure 3.11: The region and direction of the line scanning (a), and graph of EDS data from line scanning (b).

The XRD pattern of M12 alloy is presented in Figure 3.12. The XRD analysis indicates that as-cast M-12 alloy has multi-phase structure consisting of BCC, B2, $AlNi_3$, and Fe_4V phases. It is clear that the formation of second phases is due to the V alloying. The SEM images of M-12 alloy is presented in Figure 3.13 (a, b, c, and d). M-12 alloy exhibits two phases structure as cubical phase distributed through the matrix. The distribution of the second phase is seen both through grain boundaries and into the grains.

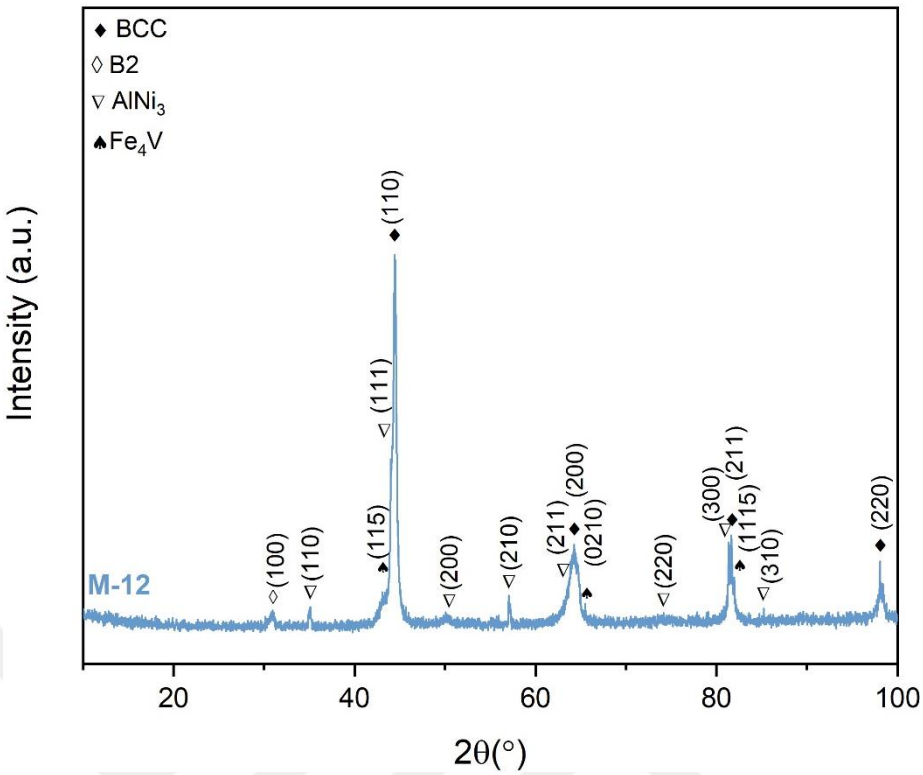

Figure 3.12:XRD pattern of M-12.

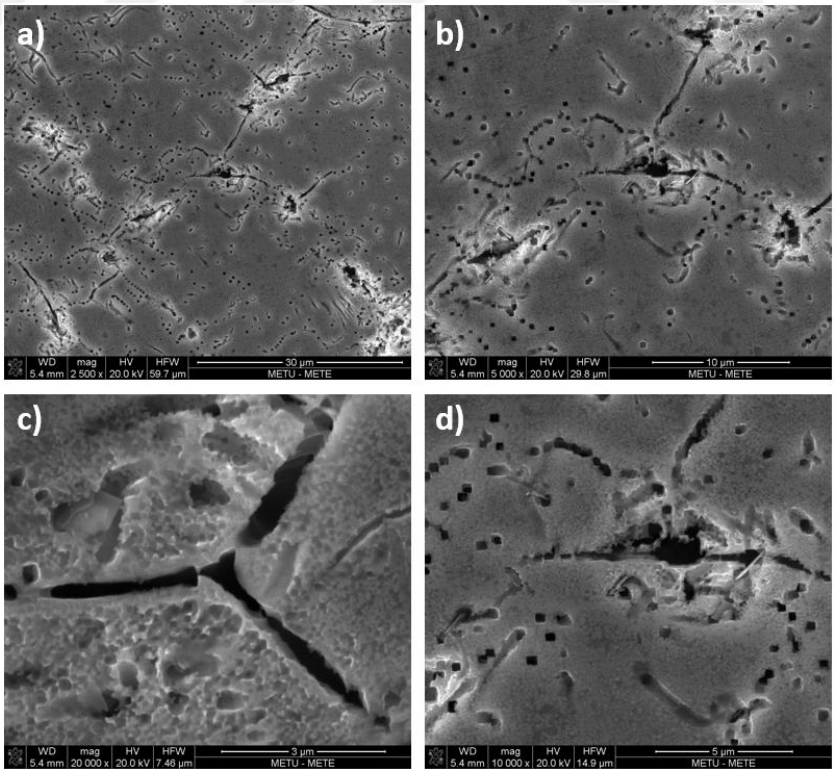

Figure 3.13: SEM images of M-12 at different magnifications.

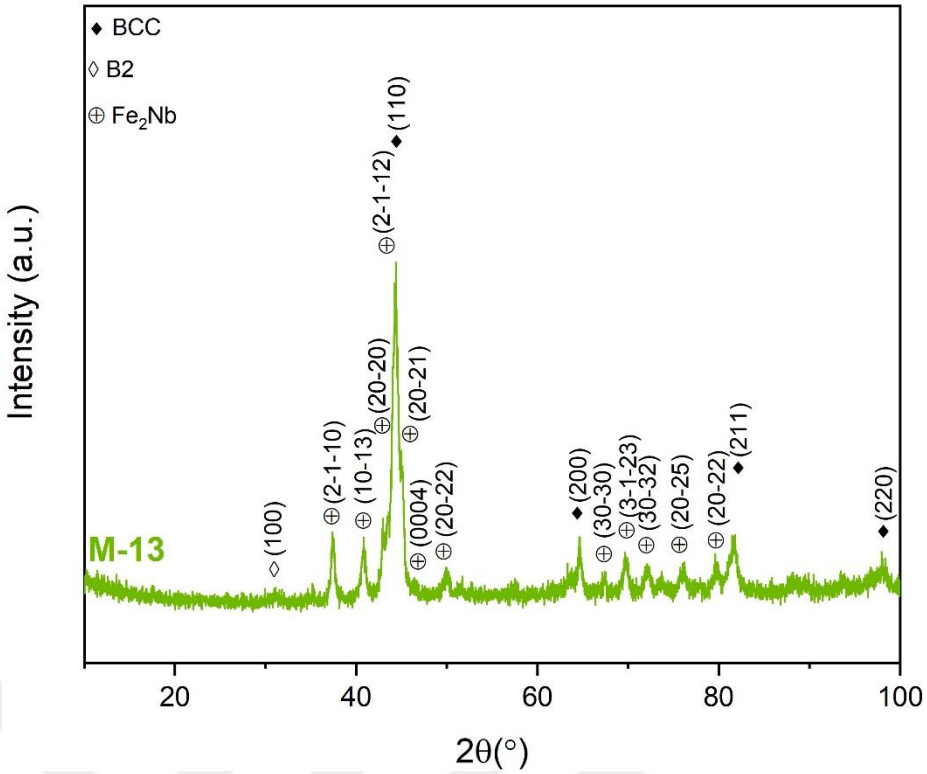

Figure 3.14: XRD pattern of M-13 alloy.

The XRD pattern of M-13 alloy is presented in Figure 3.14. V element is replaced with Nb element in M-13 alloy as a different from M-12 alloy. XRD analysis indicates the formation of BCC, B2, and Fe_2NB phases. Fe2Nb phase is a cubic laves phase. The SEM images of M-13 alloy is presented in Figure 3.15 (a, b, c, and d). M-13 alloy exhibit two phases structure, which are matrixes and dendritic regions between grains. The directions and region of line and collected data are presented in Figure 3.16 (a) and (b) respectively. The line scanning EDS results indicate that Nb is higher at matrix, while Al, Cu, and Ni are higher at dendritic regions.

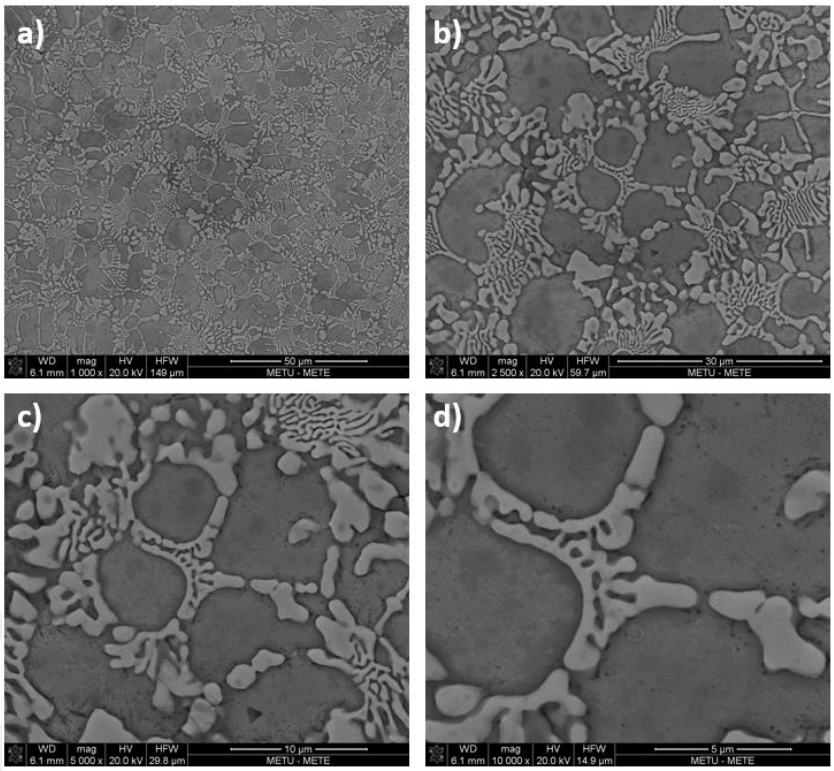

Figure 3.15:SEM images of M-13 alloy at different magnifications.

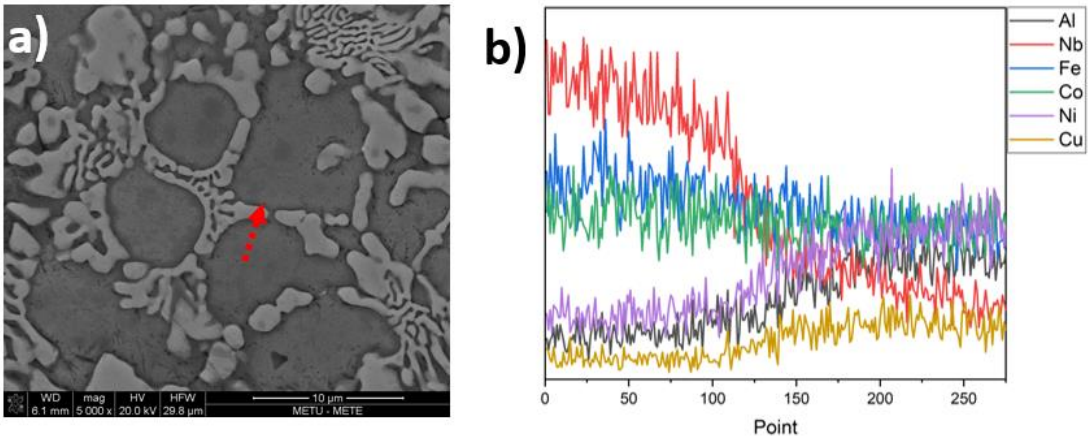

Figure 3.16:SEM image and line scanning analysis (a), and graph of EDS data from line scanning (b).

3.3 MAGNETIC CHARACTERIZATION

Magnetic properties of the HEAs were investigated using vibrating sample magnetometer (VSM). VSM analysis gives the information about saturation magnetization (M_s), remanent magnetization (M_r), and coercivity (H_c) of the alloys. Figure 3.17 illustrates hystersis loops, achieved from VSM analysis, for M-01, M-02, and M-03 alloys. It is observed that M-01 alloy has the highest H_c while the highest M_r value is seen for M-03 alloy and M-02 alloy has the highest M_s value. It is seen

that increase in Co addition decreases the coercive force and increases the magnetic saturation of the alloys. M-02 and M-03 alloys have higher Co ratio than M-01 The amount of decrease in the coercive force and increase in the magnetic saturation are reduced by changing Cu and Ti ratio in the alloys. While Co concentration decreases the coercive forces and increases the magnetic saturation, Cu and Ti concentrations have opposite effects on these properties.

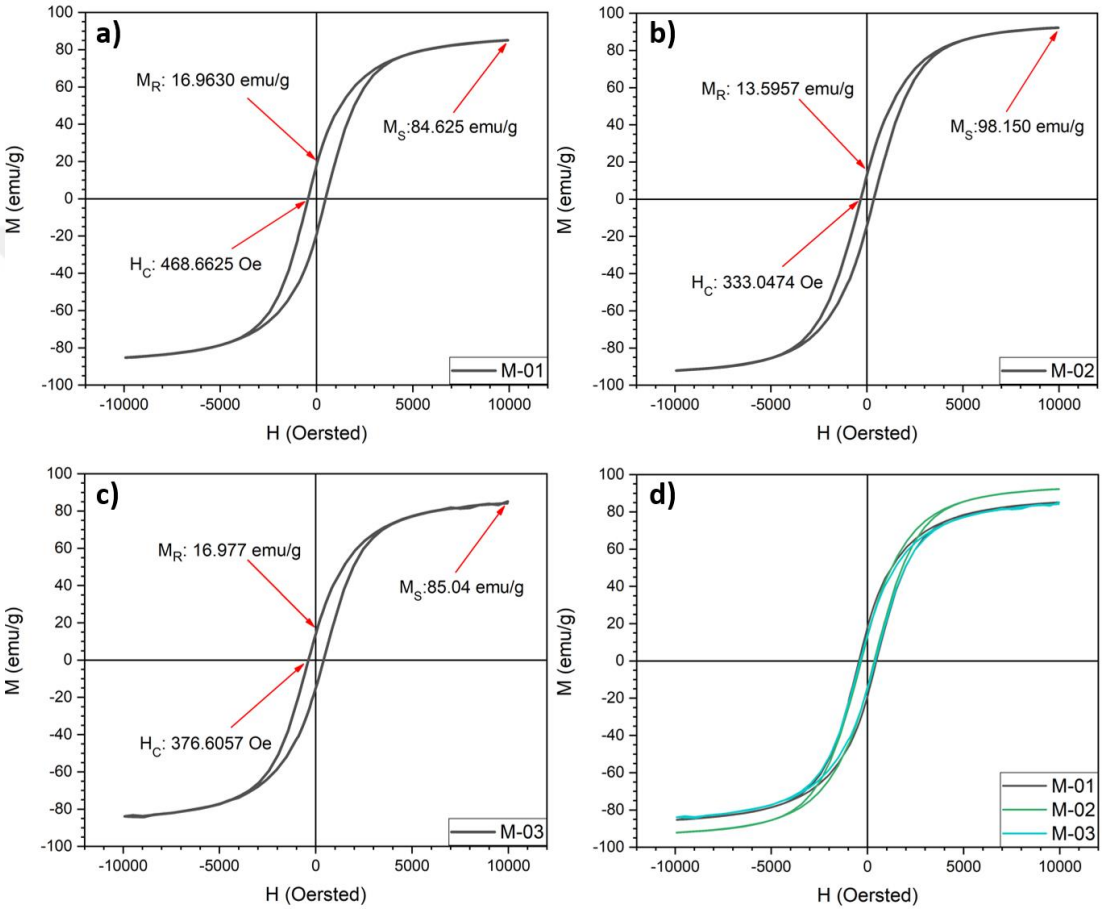

Figure 3.17: Hysteresis loops of M-01(a), M-02 (b), and M-03 (c). Overlayed hysteresis loops of M-01, M-02, and M-03 (d).

The hysteresis loops of as-cast M-01 and isothermally annealed at 928 K for 3 hours M-01-3HT, and for 24 hours M-01-24HT alloys are shown in Figure 6. It is seen that while the coercive force of M-01-3HT alloy decreases, its residual magnetism slightly decreases after 3 hours of annealing. Furthermore, it is observed that magnetic saturation of M-01 alloy increases after 3 hours of isothermal annealing. Changing the annealing time effects the magnetic properties. M-01-24HT alloy shows higher coercive force and residual magnetism than that of the as-cast M-

01 and M-01-3HT, the magnetic saturation decreases. Table 3.6 tabulates the magnetic properties of these alloys.

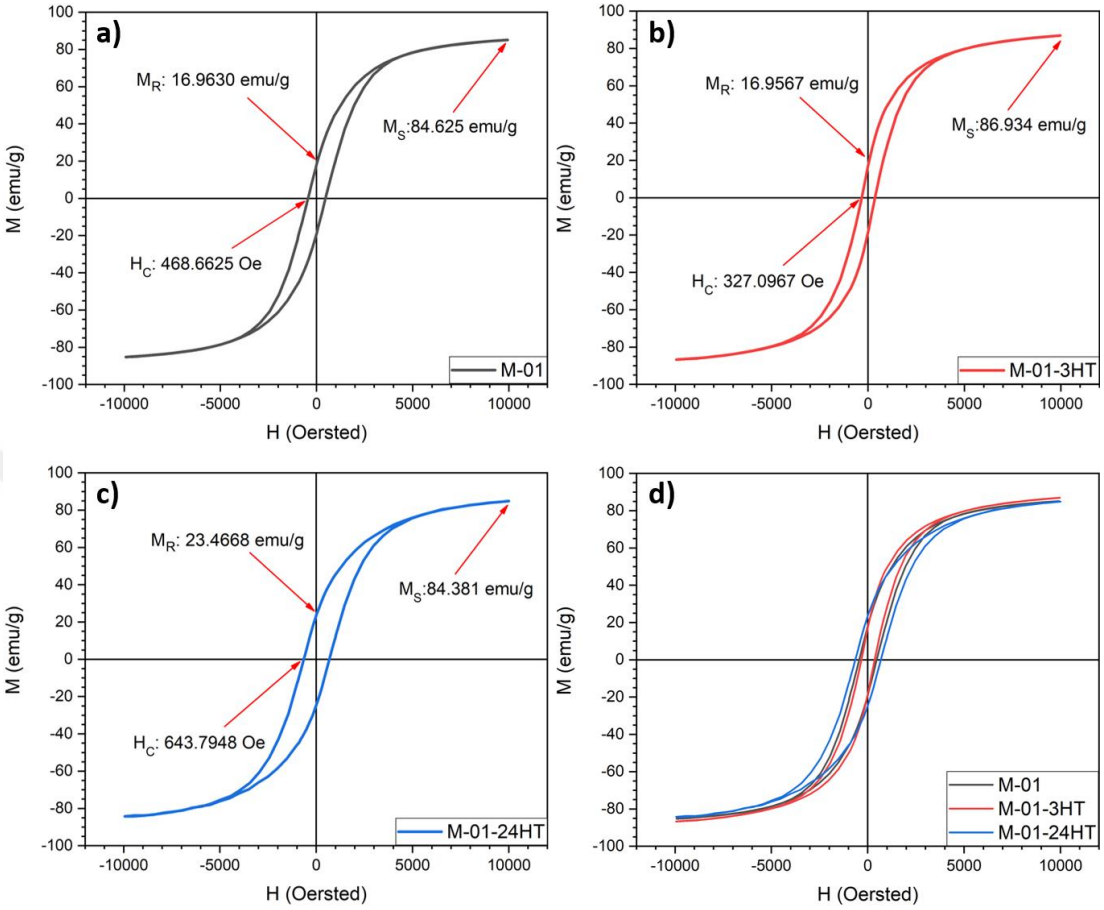

Figure 3.18: Hysteresis loops of M-01 (a), M-01-3HT (b), and M-01-24HT (c). Overlayed hysteresis loops of M-01, M-01-3HT, and M-01-24HT (d).

Hysteresis loops of M-02 alloys are presented in Figure 3.18 (b). It was mentioned before, M-02 alloy has higher magnetic saturation than M-01 alloy. However, coercive force and residual magnetism values of M-02 alloy as not good enough as that of M-01 alloy. The increase in coercive force and residual magnetism was observed for M-02-3HT alloy. The coercive force of M-02-3HT increases more than double of that of M-02 alloy. On the other hand, residual magnetism also increases, but as much as coercive force. Besides the increase in both coercive forces and residual magnetism, there is a decrease in magnetic saturation of M-02-3HT alloy.

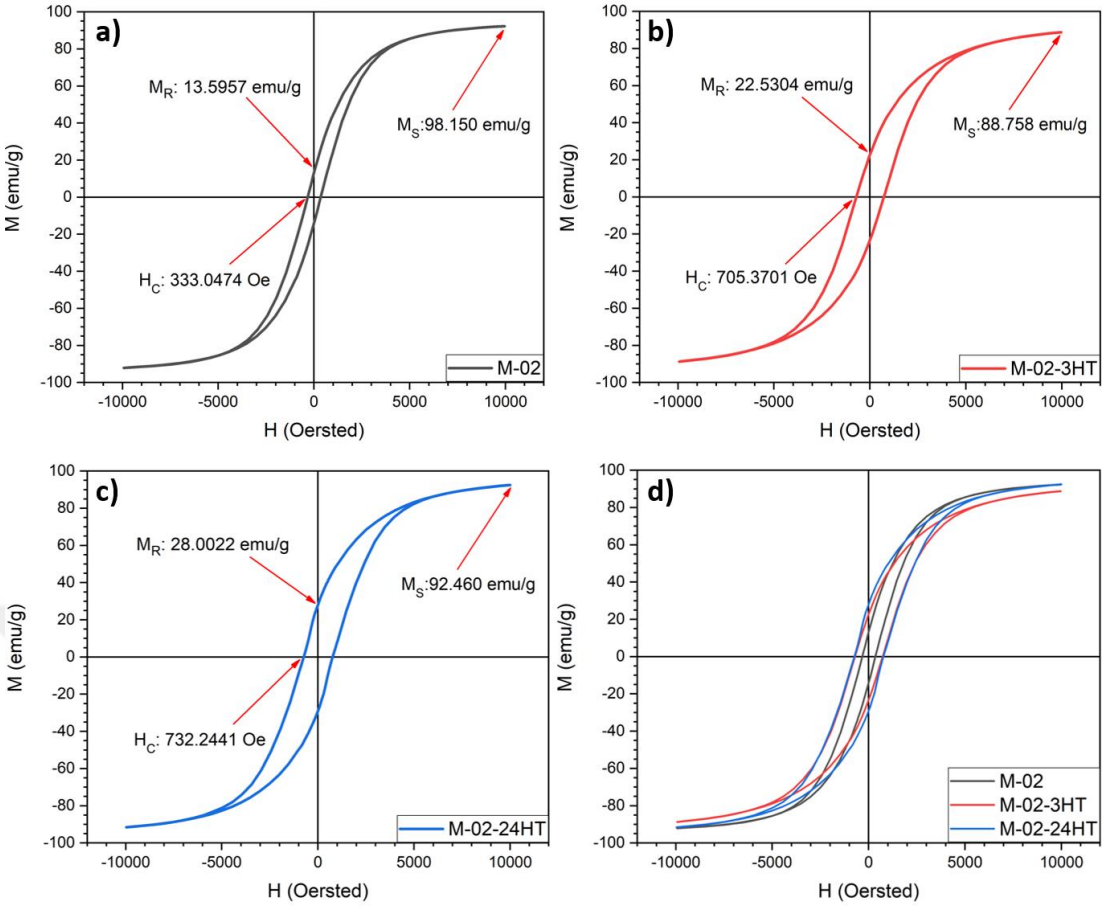

Figure 3.19: Hysteresis loops of M-02 (a), M-02-3HT (b), and M-02-24HT (c). Overlayed hysteresis loops of M-02, M-02-3HT, and M-02-24HT (d).

Figure 3.19 (c) indicates the hysteresis loops for in M-02-24HT alloy. It is observed that after the 24 hours isothermal annealing at 928 K, the coercive force, residual magnetism, and magnetic saturation are increasing. Coercive force and residual magnetism of M-02-24HT are higher than that of M-02-3HT alloy. The coercive force and residual magnetism of M-02-24HT increase as 119.86% and 105.96% compared to the increase of coercive force and residual magnetism of M-02 alloy, respectively. The magnetic saturation of M-02-24HT alloy is higher than that of M-02-3HT alloy, but it is lower than the magnetic saturation of as-cast M-02 alloy. The analysis shows that M-02-24HT has the highest value of residual magnetism. It is clear that the coercive force and the residual magnetism as-cast M-02 alloy increase with isothermal annealing and especially with the isothermal annealing for 24 hours. This is probably due to the phase transformation and the formation of new phases with annealing. The structural changes decrease the magnetic saturation for of M-02-24HT alloy. The isothermal annealing time is also effective on the magnetic properties, for instance annealing for 3 hours does not

create structural changes as much as 24 hours of annealing. Therefore, significant changes in structure and the magnetic properties of the alloys occur for longer annealing times.

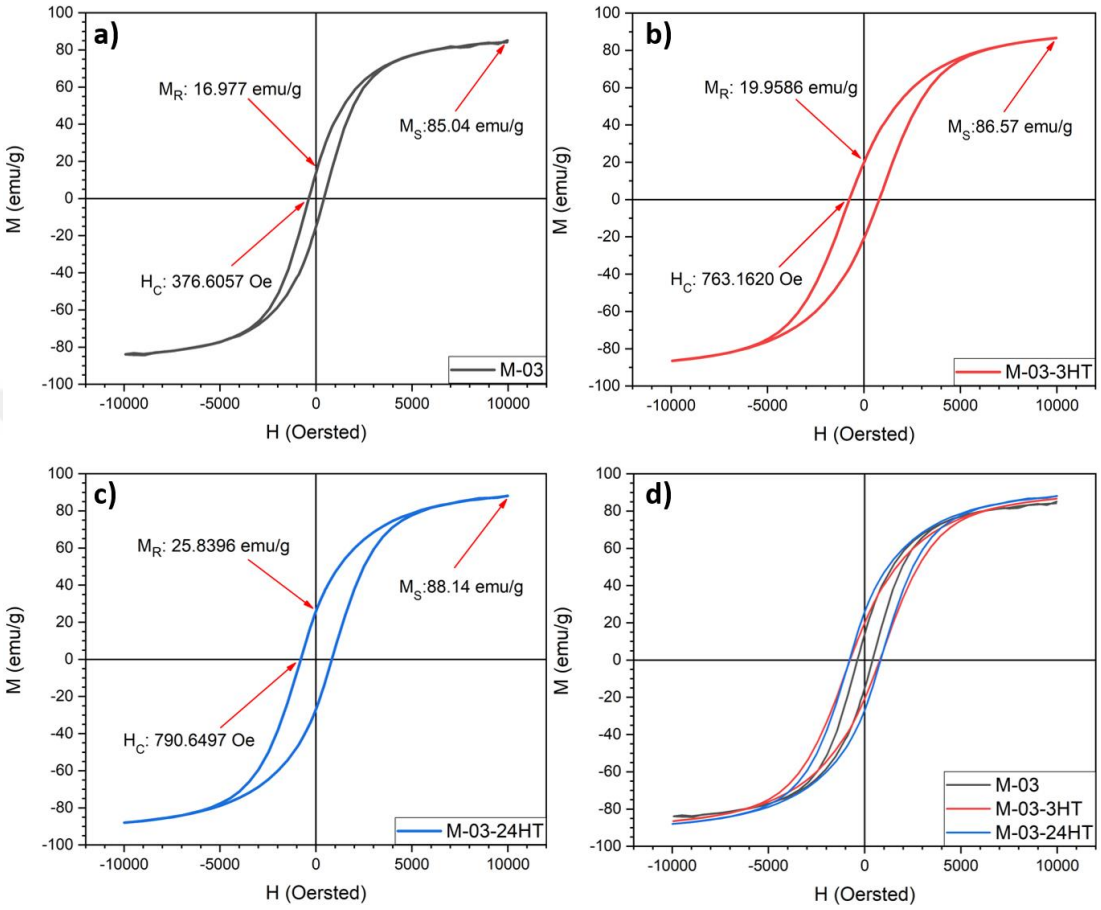

Figure 3.20: Hysteresis loops of M-03 (a), M-03-3HT (b), and M-03-24HT (c). Overlayed hysteresis loops of M-03, M-03-3HT, and M-03-24HT (d).

Hysteresis loops of M-03 alloys are presented in Figure 3.20. As it was mentioned before, M-03 alloy have lower H_c, and nearly same M_r and M_s values than M-01 alloy. On the other hand, it has higher H_c and M_r values than M-02 alloy. The increase in magnetic properties was observed after isothermally annealed for 3 hours of M-03. The coercive force of M-03-3HT increased more than doubled of that of M-03. The coercive force of M-03-3HT alloy increased as 102.64 % than M-03. On the other hand, residual magnetism also increased, but not as much as coercive force. The residual magnetism value increased from 16.977 to 19.9586 emu/g. In addition to both increases, a slightly increase in magnetic saturation of M-03-3HT was observed. Although M-03-3HT has higher coercive force value than M-02-3HT, the residual magnetism value is lower. In contrast to M-02-3HT alloy, the increase in

saturation magnetism of M-03-3HT alloy was also observed. That is, M-03-3HT alloy shows increasing in each property.

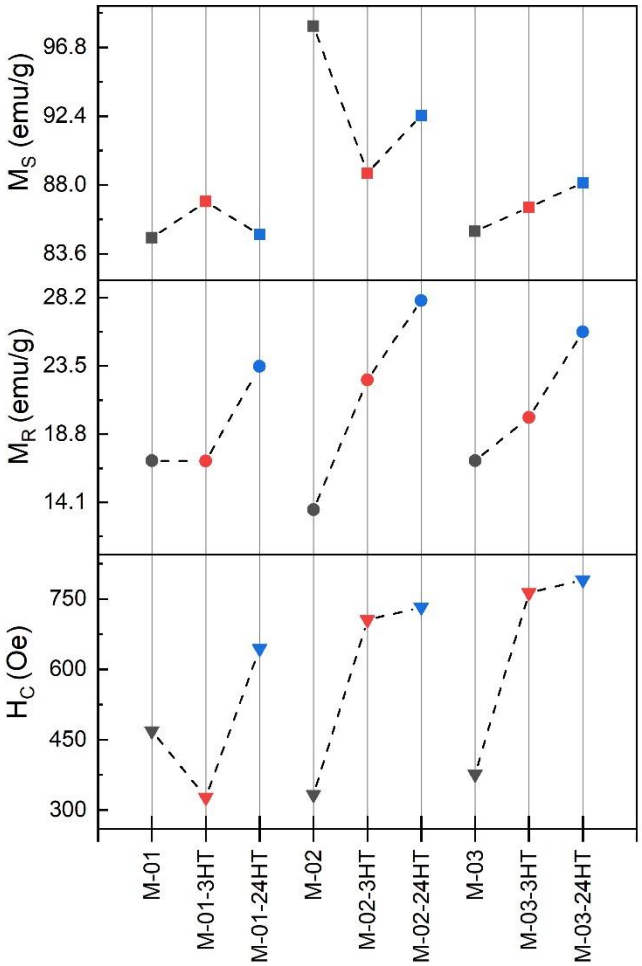

Figure 3.21: Comparison graphs of HC, MR, and MS values of M-01, M-02, and M-03 sample series.

Figure 3.20 (c) indicates the hysteresis loops for in M-03-24HT alloy. It is observed that after the 24 hours isothermal annealing at 928 K, the coercive force, residual magnetism, and magnetic saturation are increasing. Coercive force, residual magnetism, and magnetic saturation of M-03-24HT are higher than that of M-03-3HT alloy. The increases in coercive forces of M-03-3HT and M-03-24HT are 102.64% and 109.94%, respectively. The increases in coercive forces of M-03-3HT and M-03-24HT are 17.56% and 52.20%, respectively. The increases in residual magnetism of M-03-3HT and M-03-24HT are lower than M-02-3HT and M-02-24HT.

M-03 alloys show the best improvement in each magnetic property among other alloys. M-03-3HT and M-03-24HT alloys have lower amount of improvement

coercive forces and residual magnetisms than that of M-02-3HT and M-02-24HT alloys. The amounts of increase in coercive forces of M-03-3HT and M-03-24HT are calculated as 102.64% and 109.94%, respectively. The changes in the coercive forces are more than double. The amount of increase in the residual magnetism are 17.56% and 52.20%. Residual magnetism value of M-03-24HT did not reach the double as same as the M-02-24HT. Although the M-02 alloys are showing the highest increases, M-03 alloys shows increasing in every property.

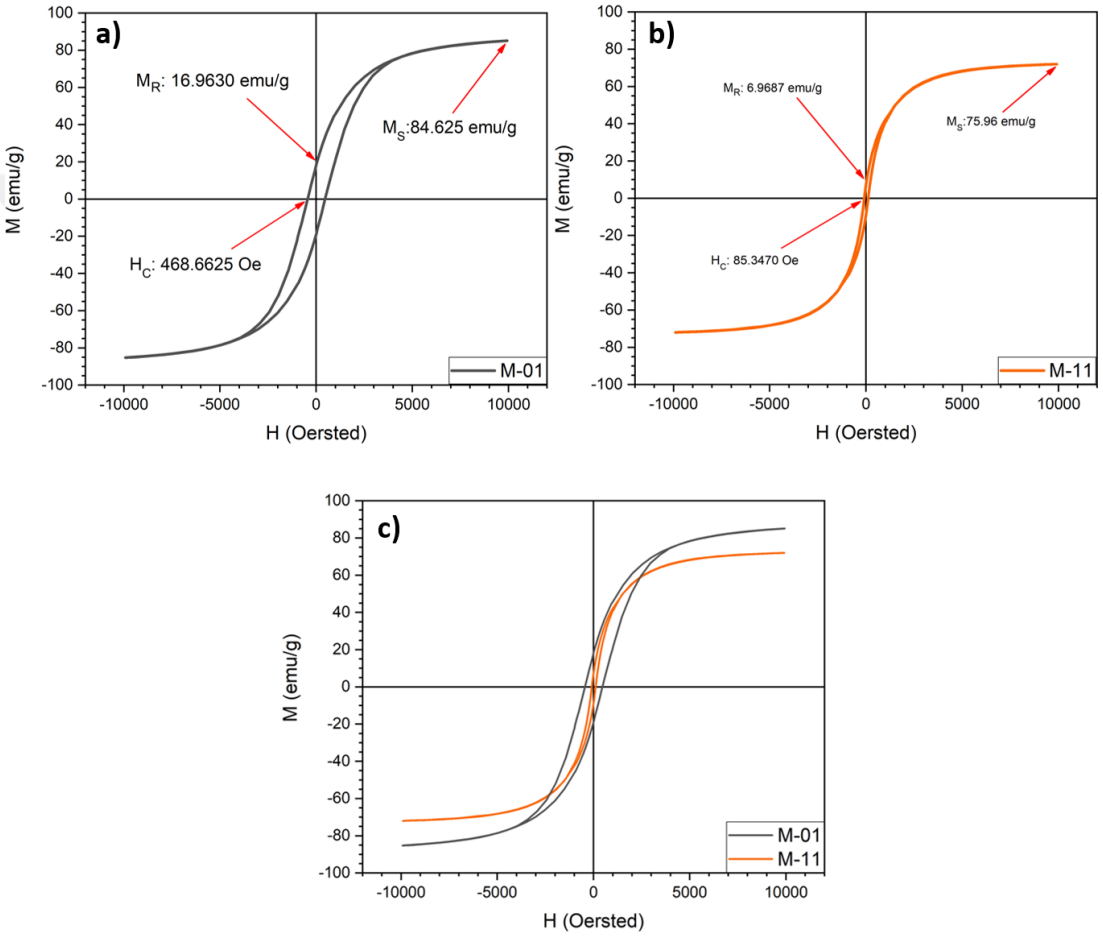

Figure 3.22: Hysteresis loops of M-01 (a) and M-11 (b). Overlayed hysteresis loops of M-01 and M-11 (c).

Figure 3.21 illustrates hysteresis loops, achieved from VSM analysis, for M-01and M-11 alloys. M-11 is an equiatomic alloy and it has not Ti element in system. The composition of M-11 is equiatomic and it does not contain Ti element in system. The coercive force of M-11 is much lower than M-01 alloy. It is clear that the formation of BCC structure increases magnetic properties of alloys. Addition of Ti

element induce to formation of BCC structure. Besides to this, the decrease in Fe ratio is also effective on the decreases in magnetic properties.

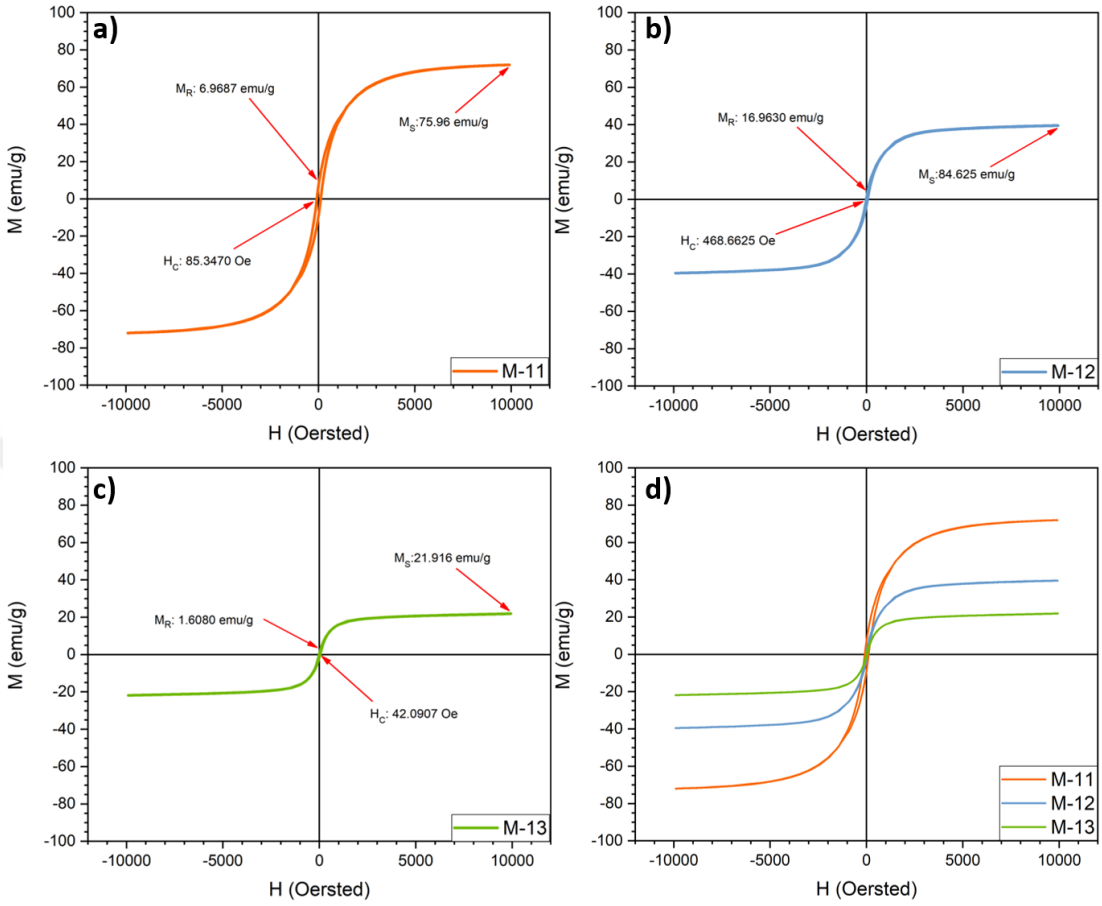

Figure 3.23: Hysteresis loops of M-11(a), M-12 (b), and M-13 (c). Overlayed hysteresis loops of M-11, M-12, and M-13 (d).

Figure 3.22 (b) indicates the V added M-12 alloy. The decreases in coercive force, residual magnetism, and magnetic saturation were observed after addition of V element to M-12 alloy. The ratio of decrease in coercive force, residual magnetism, and magnetic saturation are 34.27%, 53.39%, and 48.08% respectively. It is clear that addition of V cause to reduction in magnetic properties due to triggered to formation of second phases in system.

Figure 3.22 (c) indicates the Nb added M-13 alloy. The decreases in coercive force, residual magnetism, and magnetic saturation were observed after addition of Nb element to M-13 alloy similar to M-12 alloy. The ratio of decrease in coercive force, residual magnetism, and magnetic saturation are 50.68%, 76.92%, and 71.16% respectively. M-13 alloy has the lowest magnetic properties among all alloys. It is clear that addition of Nb cause to reduction in magnetic properties due to triggered to

formation of second phases in system, similar to addition of V element. Both addition of V and Nb affect to decreases in amount of the BCC structure and this cause to decreases in the magnetic properties. Magnetic properties and elemental formulas of all alloys are given in Table 3.11.

Table 3.7: Magnetic property table of samples.

Alloy	Formula	H_C (Oe)	M_R (emu/g)	M_S (emu/g)
M-01	$Fe_2CoNiAlCu_{0.4}Ti_{0.4}$	468.6625	16.9630	84.625
M-01-3HT		327.0967	16.9567	86.934
M-01-24HT		643.7948	23.4668	84.831
M-02	$Fe_2Co_{1.5}NiAlCu_{0.4}Ti_{0.4}$	333.0474	13.5957	98.150
M-02-3HT		705.3701	22.5304	88.758
M-02-3HT		732.2441	28.0022	92.460
M-03	$Fe_2Co_{1.5}NiAlCu_{0.5}Ti_{0.5}$	376.6057	16.977	85.04
M-03-3HT		763.1620	19.9586	86.57
M-03-24HT		790.6497	25.8396	88.14
M-11	FeCoNiAlCu	85.3470	6.9687	75.96
M-12	$FeCoNiAlCu_{0.5}V_{0.5}$	56.0988	3.2484	39.44
M-13	$FeCoNiAlCu_{0.5}Nb_{0.5}$	42.0907	1.6080	21.91

3.4 MECHANICAL PROPERTIES

Mechanical properties of the alloys are significantly affecting the application of HEAs for magnetic purposes in terms of their usability and workability. The Vickers microhardness tests of the HEAs were performed using hardness tester. The hardness values of the alloys give information about their machinability and brittleness. The structural and microstructure changes due to elemental ratio changes or phase transformations with annealing have huge impact on the hardness values of the alloys. The hardness of as-cast M01 alloy was measured as 653.17 ±21.347 HV which is triple of the hardness of 1040 steel. It is clear that the formation of BCC structure increases hardness of the alloys. The isothermally annealed M-01 alloy for 3 hours show higher hardness value than that of the as-cast M-01 alloy. There is no structural change in M-01 alloy after annealing for 3 hours. The hardness values are decreasing with 24 hours of isothermal annealing due to the phase transformation and the formation of second phase.

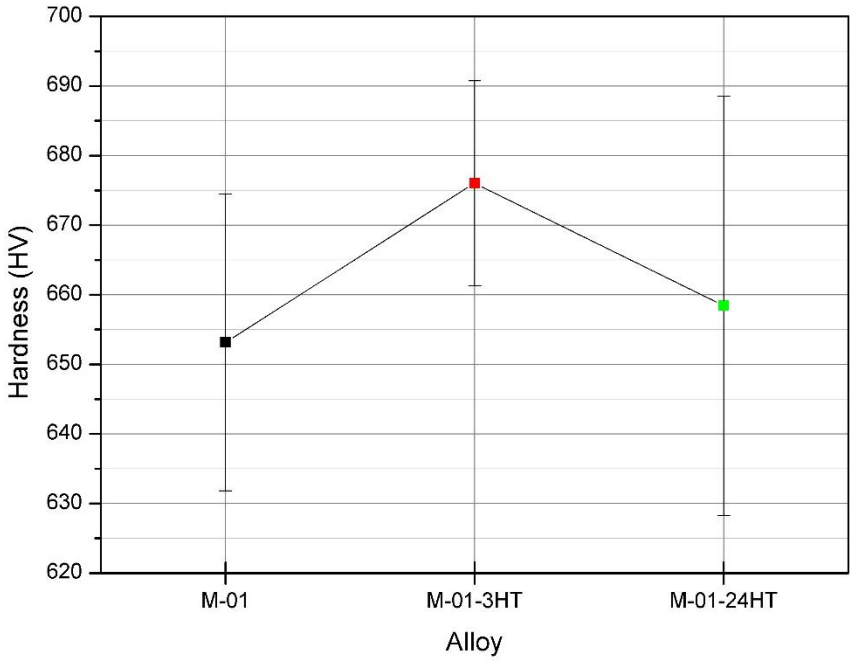

Figure 3.24: Vickers microhardness plots of as-cast M-01 alloy, and isothermally annealed M-01-3HT, and M-01-24HTalloys at 928 K for 3 and 24 hours, respectively.

The hardness of as-cast M01 alloy was measured as 653.17 ±21.347 HV which is triple of the hardness of 1040 steel. It is clear that the formation of BCC structure increases hardness of the alloys. The isothermally annealed M-01 alloy for 3 hours show higher hardness value than that of the as-cast M-01 alloy. There is no structural change in M-01 alloy after annealing for 3 hours. The hardness values are decreasing with 24 hours of isothermal annealing due to the phase transformation and the formation of second phase.

The hardness of as-cast M-02 was found as 651.19 ±20.96 HV which is similar to as-cast M-01. As it was mentioned before, the BCC structure formation affected the hardness of alloys. The isothermally annealed M-02 alloy for 3 hours exhibit higher hardness value than that of the as-cast M-02 alloy. M-02-3HT has the highest hardness of 718.88 ±25.417 HV among all alloys. There is no structural change in M-02 alloy after annealing for 3 hours similar to M-01-3HT alloy. The hardness of M-02 alloy decreases after isothermal annealing at 928 K for 24 hours due to the phase transformation observed similar to M-01-24HT.

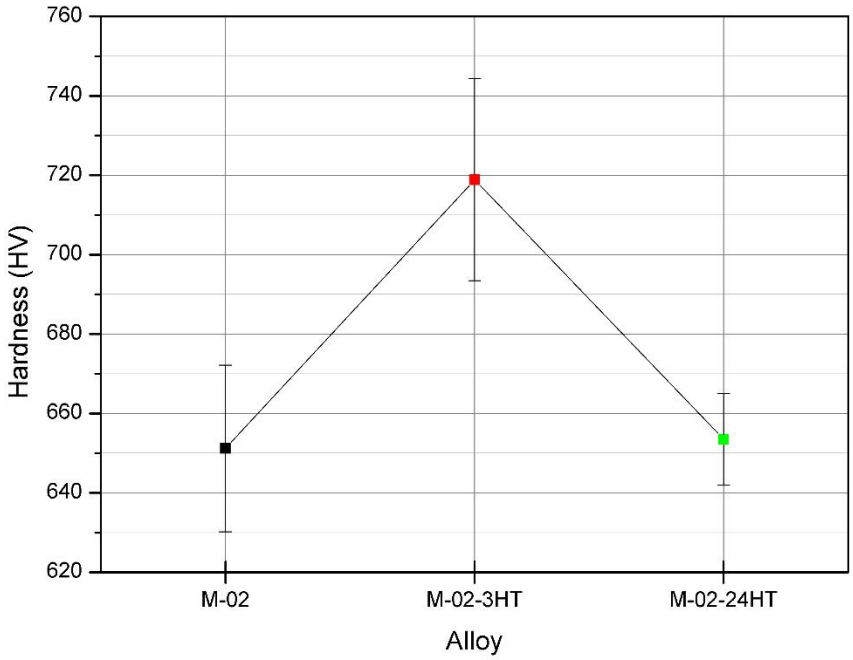

Figure 3.25: Vickers microhardness plots of as-cast M-02 alloy, and isothermally annealed M-02-3HT, and M-02-24HTalloys at 928 K for 3 and 24 hours, respectively.

The hardness of as-cast M-03 was calculated as 649.87 ±34.138 HV, which is very close to the as-cast M-01 and M-02 alloys. Regarding their BCC structure, as-cast alloys show similar hardness values. M-02-3HT alloy, which for isothermally annealed for 3 hours, shows higher hardness value than as-cast M-03 alloy. Moreover, there is a decrease in hardness value of M-03 alloy after isothermally annealed for 24 hours due to the phase transformation and formation of second phases similar to other alloys.

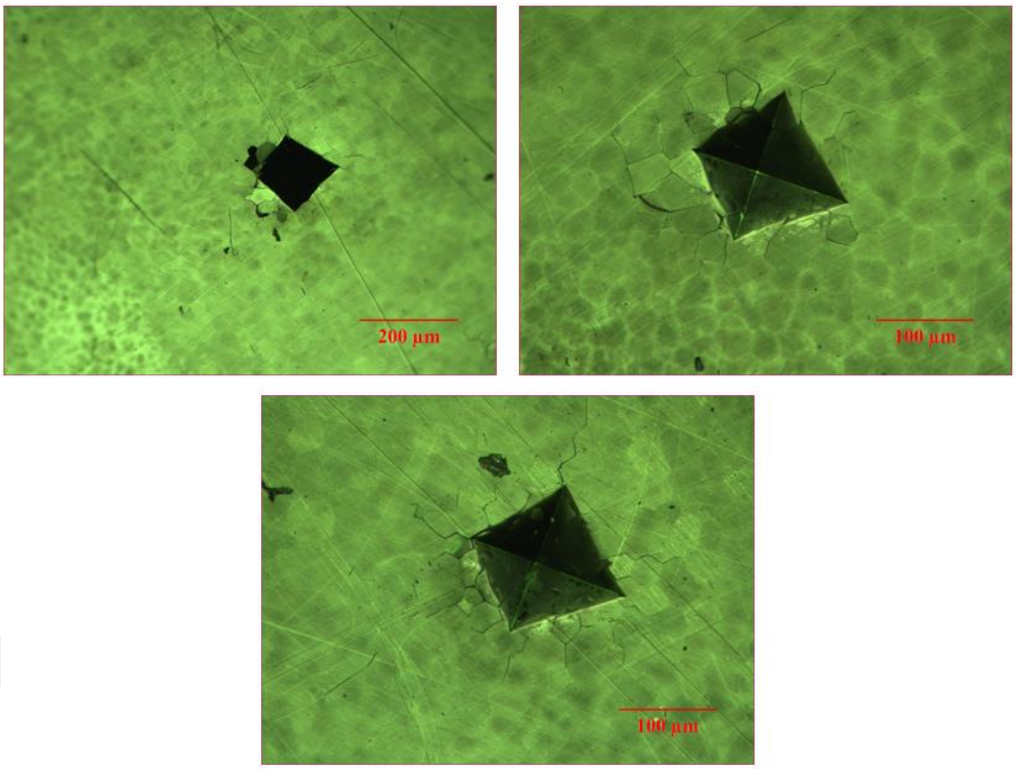

Figure 3.26:OM images of intergranular cracks on M-01-3HT.

Figure 3.26 indicates the OM images of M-01HT alloy during hardness test. The cracks due to indentation can be observed from the images due to it very brittle character.

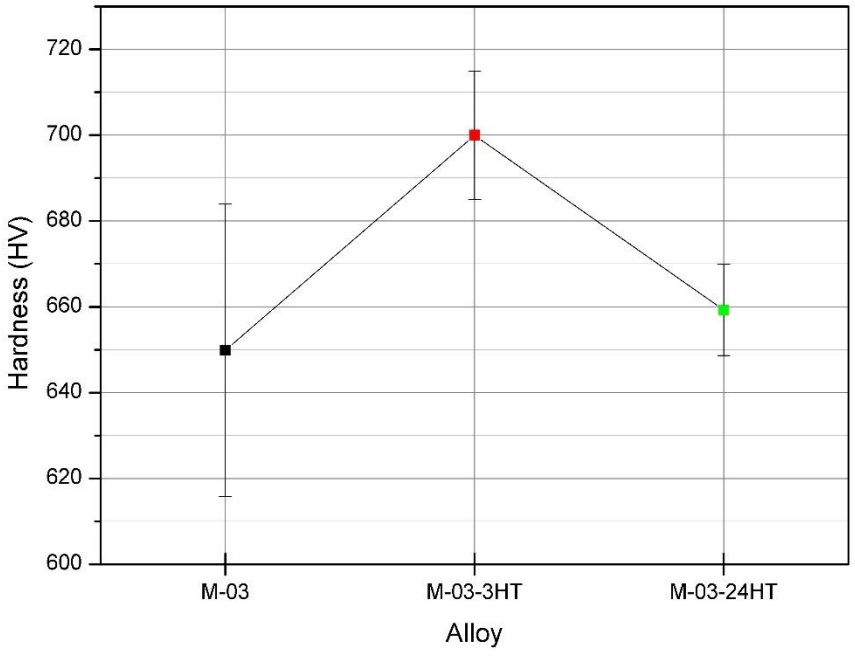

Figure 3.27: Vickers microhardness plots of as-cast M-03 alloy, and isothermally annealed M-03-3HT, and M-03-24HTalloys at 928 K for 3 and 24 hours, respectively.

The hardness value of M-11 was measured as 455.16 ±14,658 HV which is double of the hardness of 1040 steels. It is clear that the formation of the FCC structure decreases the hardness of this alloy. The hardness of M-12 alloy was found as 445.07 ±14.078 HV, and it is close to M-11 alloy. Although phase transformation and precipitation occur after the addition of V, there is notable changes observed in the hardness value of M-12 alloy. The hardness value of M-13 was measured as 681.91 ±13.483 HV. It is observed that the addition of Nb element increases hardness of M-13 alloy. The hardness value of M-13 alloy is similar to M-01-3HT, M-02-3HT, and M-03-3HT alloys, and it is triple of the hardness of 1040 steels.

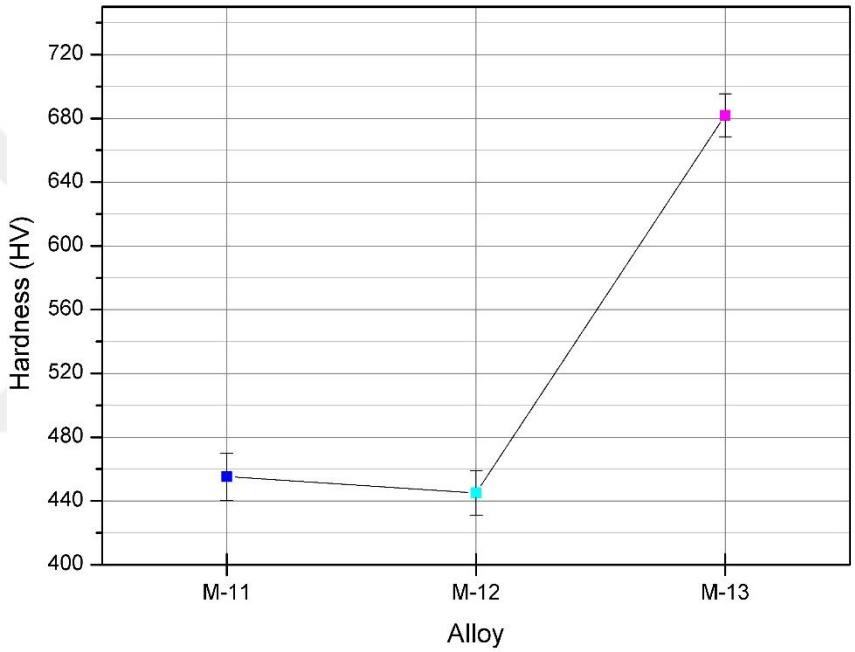

Figure 3.28: Vickers microhardness plots of as-cast M-11, M-12, and M-13 alloys.

CHAPTER IV

4. CONCULISION AND FUTURE PREDICTIONS

4.1 CONCULISION

This thesis focused on the synthesis and development of magnetic high entropy alloys. This study focused on Fe-Co-Ni-Al-Cu-X (X: Ti, V, Nb) high entropy alloy. The alloy design was performed due to thermodynamic data calculations and selection of constituent elements that show magnetic properties. The alloy systems were produced using vacuum arc melting technique from high-purity elements. The high entropy alloys were characterized using X-ray diffraction (XRD), optical microscope (OM), scanning electron microscope (SEM), energy dispersive spectroscopy (EDS), vibrating sample magnetometer (VSM), and hardness tester. The conclusions of this thesis can be given as

- The XRD analysis of as-cast M-01, M-02, and M-03 alloys show single BCC phase formation, however the VEC calculations show dual-phase structure for these alloys. It is clear that VEC calculations are not enough for crystal structure determination of HEAs.
- The equiaxed morphology were observed for as-cast and isothermally annealed M-01, M-02, M-03 at 928 K for 3 hours HEAs.
- The phase transformation of M-01, M-02, M-03 HEAs were observed after 24 hours isothermal annealing at 928 K.
- The microstructure of M-01, M-02, M-03 HEAs were changed from equiaxed to dendritic morphology isothermal annealing at 928 K for 24 hours. Phase formation and microstructure morphology of M-01, M-02, and M-03 alloys are similar to each other.
- M-02-3HT, M-03-3HT, M-01-24HT, M-02-24HT, and M-03-24HT HEAs exhibit hard magnetic behaviors. The XRD patterns of M-11 alloy show dual-phase FCC+BCC structure consisting with VEC calculations.
- The V addition M-12 alloy results in changes in microstructure and phase formation mechanism. The XRD pattern of M-12 alloy shows

- intermetallic phase formation can be observed XRD pattern of M-12.SEM analysis of M-12 alloy indicates the formation of precipitations with V addition.
- Nb-addition changes the microstructure and phase formation mechanism of M-13 alloy
- The saturation magnetization of M-02 and M-03 alloys increase with increasing the Co concentration in M-01 alloy
- The Co-addition decrease the coercive forces of the alloys.
- Higher coercive forces and residual magnetization were observed for the isothermally annealed alloys with higher Co concentrations.
- M-02 HEA shows show the best magnetic properties.
- M-03-24HT inhibits the highest coercive force value of 790.6497 Oe. M-02-24HT inhibits the highest residual magnetism value of 28,0022 emu/g. M-02 inhibits the highest magnetic saturation value of 98,150 emu/g.
- The magnetic properties of the alloys are negatively affected by the addition of V and Nb. The Vickers microhardness values of as-cast and isothermally annealed M-01, M-02, and M-03 alloys exhibit similar hardness values.
- M-11 HEA alloy shows the lowest hardness value.
- The addition of Nb was found to increase the hardness values critically
- M-02-24HT alloy indicates the best magnetic properties, such as highest residual magnetism value, good coercive force, and magnetic saturation.

4.2 FUTURE PREDICTIONS

According to the findings of this work, future recommendations can be suggested as follows:

- The thermal analysis such as TGA or DSC can be performed to investigate the Curie temperatures of M-02-24HT and M-03-24HT alloys that show the best magnetic properties.
- The mechanical tests, such as tensile or compressive can be applied to obtain more information about the mechanical properties of alloys.
- New alloys with various Co and/or Cu/Ti concentrations can be designed to investigate the effect of these elements.

- The phase stability and magnetic properties of M-01, M-02, and M-03 alloys can be investigated using in-situ XRD.
- The corrosion tests of the alloys can be performed to determine their corrosive properties.
- M-02-24HT and M-03-24HT alloys with good magnetic properties can be produced as a polymer matrix metal composite and developed for potential uses in electric machines.

REFERENCES

[1] GEORGE Eosa P., RAABE Dierk and RITCHIE Robert O. (2019), "High-entropy alloys", *Nature Review Materials*, vol. 4, no. 8, pp. 515–534.

[2] YEH Jien-Wei, CHEN Swe Kai, LIN Su Jien, GAN Jon Yiew, CHIN Tsung Shune, SHUN Tao Tsung, TSAU Chun Huei and CHANG Shou Yi (2004), "Nanostructured high-entropy alloys with multiple principal elements: Novel alloy design concepts and outcomes", *Advance Engineering Materials*, vol. 6, no. 5, pp. 299–303.

[3] MURTY Bhagevatula Satyanarayana, YEH Jien-Wei, RANGANATHAN Srinivasa and BHATTACHARJEE Pinaki Prasad (2019), *High-Entropy Alloys*, Second Edition, Elsevier, Amsterdam.

[4] WOO Wanchuck, HUANG E. Wen, YEH Jien-Wei, CHOO Hahn, LEE Chi and TU Shan Yi (2015), "In-situ neutron diffraction studies on high-temperature deformation behavior in a CoCrFeMnNi high entropy alloy", *Intermetallics*, vol. 62, pp. 1–6.

[5] CHEN Jian, ZHOU Xueyang, WANG Weili, LIU Bing, LV Yukun, YANG Wei, XU Dapeng and LIU Yong (2018), "A review on fundamental of high entropy alloys with promising high–temperature properties", *Journal of Alloys and Compounds*, vol. 760, pp. 15–30.

[6] CALVO-DAHLBORG Monique and BROWN S. G. R. (2017), "Hume-Rothery for HEA classification and self-organizing map for phases and properties prediction", *Journal of Alloys and Compounds*, vol. 724, pp. 353–364.

[7] TROPAREVSKY M. Claudia, Morris James R., DAENE Markus, WANG Yang, LUPINI Andrew R. and STOCKS G. Malcolm (2015), "Beyond Atomic Sizes and Hume-Rothery Rules: Understanding and Predicting High-Entropy Alloys", *Jom*, vol. 67, no. 10, pp. 2350–2363.

[8] KUMARI Priyanka, GUPTA Amit K., MISHRA Rajesh K., AHMAD M. S. and SHAHI Rohit R. (2022), "A Comprehensive Review: RecentProgress on Magnetic High Entropy Alloys and Oxides", *Journal of Magnetism and Magnetic Materials*, vol. 554, no. July 2021, pp. 169142.

[9] LEONG Zhaoyuan, WRÓBEL Jan S., DUDAREV Sergei L., GOODALL Russell, TODD Iain and NGUYEN-MANH Duc (2017), "The Effect of Electronic Structure on the Phases Present in High Entropy Alloys", *Scientific Reports*, vol. 7, no. July 2016, pp. 1–12.

[10] TSAI Ming Hung and YEH Jien-Wei (2014), "High-entropy alloys: A critical review", *Materials Research Letters*, vol. 2, no. 3, pp. 107–123.

[11] YEH Jien-Wei (2013), "Alloy design strategies and future trends in high-entropy alloys", *Jom*, vol. 65, no. 12, pp. 1759–1771.

[12] TOKAREWICZ Marzena and GRĄDZKA-DAHLKE (2021), "Review of recent research on alcocrfeni high-entropy alloy", *Metals (Basel)*, vol. 11, no. 8.

[13] CALLISTER William D. and RETHWISCH David G. (2010), *Materials Science and Engineering: An Introduction*, 8th Edition, John Wiley & Sons, Versailles.

[14] CULLIY B. D. and GRAHAM C. D. (2008), *Introduction to magnetic materials*, Second Edition, John Wiley & Sons, New Jersey.

[15] TAMHANKAR R. V.and CHANDRASEKARAN S. (1975), "Recent Trends in Development of Permanent Magnets", *IETE Journal of Research*, vol. 21, no. 10, pp. 547–550.

[16] GOLL D. and KRONMÜLLER Helmunt (2000), "High-performance permanent magnets", *Naturwissenschaften*, vol. 87, no. 10, pp. 423–438.

[17] KRAMER Matthew J., MCCALLUM R. W., ANDERSON I. A., and CONSTANTINIDES Steve (2012), "Prospects for non-rare earth permanent magnets for traction motors and generators", *Jom*, vol. 64, no. 7, pp. 752–763.

[18] YI Jian Hong (2014), "Development of samarium–cobalt rare earth permanent magnetic materials", *Rare Metals*, vol. 33, no. 6, pp. 633–640.

[19] BENZ M. G. and MARTIN D. L. (2011), "Sintering of Cobalt-Rare Earth Permanent Magnets", *AIP Conference Proceedings*, vol. 5, no. 1, pp. 1082–1086.

[20] MATSUURA Yatuka (2006), “Recent development of Nd-Fe-B sintered magnets and their applications”, *Journal of Magnetism and Magnetic Materials*, vol. 303, no. 2, pp. 344–347.

[21] KIM A. S. and CAMP F. E. (1996), “High performance NdFeB magnets (invited)”, *Journal of Applied Physics*, vol. 79, no. 8, pp. 5035–5039.

[22] BAI G., GAO R. W., SUN Y., HAN G. B. and WANG B. (2007), “Study of high-coercivity sintered NdFeB magnets”, *Journal of Magnetism and Magnetic Materials*, vol. 308, no. 1, pp. 20–23.

[23] CONSTANTINIDES Steve (2012), “The Demand for Rare Earth Materials in Permanent Magnets”, *In 51st Annual Conference of Metallurgists,* vol.7546, pp. 15.

[24] CHAUDHARY Varun, CHAUDHARY Richa, BANERJEE Rajarshi and RAMANUJAN Raju V. (2021), “Accelerated and conventional development of magnetic high entropy alloys”, *Materials Today*, vol. 49, pp. 231–252.

[25] KULKARNI Raghavendra, MURTY Bhagevatula Satyanarayana and SRINIVAS V. (2018), “Study of microstructure and magnetic properties of AlNiCo(CuFe) high entropy alloy”, *Journal of Alloys and Compounds*, vol. 746, pp. 194–199.

[26] LI Panpan, WANG Anding, and LIU C. T. (2017), “Composition dependence of structure, physical and mechanical properties of FeCoNi(MnAl)x high entropy alloys”, *Intermetallics*, vol. 87, pp. 21–26.

[27] BORKAR Tushar, CHAUDHARY Varun, GWALANI Bharat, HOUDHURI Deep, MIKLER Calvin V., SONI Vishal, ALAM Talukder, RAMANUJAN Raju V. and BANERJEE Rajarshi (2017), “A Combinatorial Approach for Assessing the Magnetic Properties of High Entropy Alloys: Role of Cr in AlCoxCr1–xFeNi”, *Advanced Engineering Materials*, vol. 19, no. 8, pp. 1–13.

[28] LIU Cong, PENG Wenyi, JIANG C. S., GUO Hongmin, TAO Jun, DENG Xiaohua and CHEN Zhaoxia (2019), “Composition and phase structure dependence of mechanical and magnetic properties for AlCoCuFeNi x high entropy alloys”, *Journal of Materials Science and Technology*, vol. 35, no. 6, pp. 1175–1183.

[29] ZHAO Chendong, LI Jinshan, LIU Yudong, WANG William Yi, KOU Hongchao, BEAUGNON Eric and WANG Jun (2021), “Tailoring mechanical and magnetic properties of AlCoCrFeNi high-entropy alloy via phase transformation”, *Journal of Materials Science and Technology*, vol. 73, pp. 83–90.

[30] LIU W. H., WANG H., WU Y., LIU X. J., NIEH T. G. and LU, Z. P. (2014), “Effects of Al addition on structural evolution and tensile properties of the FeCoNiCrMn high-entropy alloy system”, *Acta Materialia*, vol. 62, no. 1, pp. 105–113.

[31] WANG Woei Ren, WANG Wei Lin, WANG Shang Chih, TSAI Yi Chia, LAI Chun Hui and YEH Jien-Wei (2012), “Effects of Al addition on the microstructure and mechanical property of Al xCoCrFeNi high-entropy alloys”, *Intermetallics*, vol. 26, pp. 44–51.

[32] CIESLAK Jakub, TOBOLA Janusz and REISSNER M. (2020), “The effect of bcc/fcc phase preference on magnetic properties of AlxCrFeCoNi high entropy alloys”, *Intermetallics*, vol. 118, pp. 106672.

[33] MISHRA Rajesh K., SAHAY P. P. and SHAHI Rohit R. (2019), “Alloying, magnetic and corrosion behavior of AlCrFeMnNiTi high entropy alloy”, *Journal of Materials Science*, vol. 54, no. 5, pp. 4433–4443.

[34] WU Zhongyuan, LI Bin, CHEN Mengya, YANG Yong, ZHENG Ruiyi, YUAN Lu, LI Zhong, TAN Xiaohua and XU Hui (2022), “Tailoring magnetic property and corrosion resistance of FeCoNiCuAl high-entropy alloy with Ce additive”, *Journal of Alloys and Compounds*, vol. 901, pp. 163665.

[35] EMRICH Martin and OPPER Detlef (2011), *XRD for the analyst*, Second Edition, PANalytical, Kassel.

[36] KHAN Hayat, YERRAMILLI Aditya S., OLIVEIRA Adrien D., PATIENCE Gregory S., BOFFITO Daria C. and ALFORD Terry L. (2020), “Experimental methods in chemical engineering : X-ray diffraction spectroscopy — XRD”, vol. 98, no. 6, pp. 1255–1266.

[37] TECH J. Anal Bioanal, CHAUHAN Ashish, and CHAUHAN Priyanka (2014), “Analytical & Bioanalytical Techniques Powder XRD Technique and its Applications in Science and Technology”, vol. 5, no. 5, pp. 1-5.

[38] EL-ALAILY T. M., EL-NIMR M. K., SAAFAN S. A., KAMEL M. M., MEAZ T. M. and ASSAR S. T. (2015) “Construction and calibration of a low cost and fully automated vibrating sample magnetometer”, *Journal of Magnetism and Magnetic Materials*, vol. 386, pp. 25–30.

[39] KIRUPAKAR B. R., VISHWANATH B. A., SREE M. Padma and DEENADAYALAN (2016), “Vibrating Sample Magnetometer and Its Application In Characterisation of Magnetic Property of the Anti Cancer Drug Magnetic Microspheres”, *International Journal of Pharmaceutics & Drug Analysis.*, vol. 4, no. 5, pp. 227–233.